

The writhing of circular cross-section rods: undersea cables to DNA supercoils

D. M. Stump, W. B. Fraser and K. E. Gates

Proc. R. Soc. Lond. A 1998 **454**, 2123-2156

doi: 10.1098/rspa.1998.0252

Email alerting service

Receive free email alerts when new articles cite this article - sign up in the box at the top right-hand corner of the article or click [here](#)

To subscribe to *Proc. R. Soc. Lond. A* go to: <http://rspa.royalsocietypublishing.org/subscriptions>

The writhing of circular cross-section rods: undersea cables to DNA supercoils

BY D. M. STUMP¹, W. B. FRASER² AND K. E. GATES¹

¹*Department of Mathematics, The University of Queensland,
St. Lucia, QLD 4072, Australia,*

²*School of Mathematics and Statistics, The University of Sydney,
NSW 2006, Australia*

Received 2 July 1997; accepted 27 October 1997

The large deflection theory of circular cross-section elastic rods is used to consider the writhing of long straight rods subjected to tension and torque, such as undersea cables, and to closed loops with inserted twist, such as DNA supercoils.

The writhed shape of the long straight rod under tension and torque is easily generated by twisting a piece of string with the fingers and consists of three separate parts: a balanced-ply region, a free end loop, and two tail regions. The solution for the rod shape in each of the regions is found. The results are then joined together to ensure continuity of the position and tangent vectors of the strand centreline through the introduction of point forces and moments at the points where the strands enter and exit the balanced ply. The results of the model are consistent with simple experiments on long braided rope.

The writhed shape of the closed loop with twist inserted between the ends prior to closure is modelled as a balanced ply joined to two end loops. The analysis combines the mechanics solution with the conservation of topological *link* to provide a simple formula which *quantitatively* predicts the approximate shape and helix angle of the supercoil. The results are in good agreement with simple experiments on rope and with available data on DNA supercoils.

Keywords: interwound supercoils; link, twist, writhe; tortuosity and writhe; large deflection rods; linear elastic rods

1. Introduction

The writhing of a twisted rod is a process familiar to almost everyone and is easily demonstrated with a piece of string that is held under tension and twisted with the fingers. As the ends are slowly displaced towards each other, the rod ‘writhes’ into the shape shown in figure 1. Greenhill (1883) showed that a ‘long’ straight rod loaded under a remote tension T_∞ and torsional moment Q_∞ first buckles into a helical shape when

$$T_\infty = \frac{Q_\infty^2}{4B},$$

where the bending rigidity $B = EI$, E is Young’s modulus and I is the second area moment of the cross-section. The helix quickly localizes into a shape which is similar to a solitary wave (Coyne 1990), and eventually the rod contacts itself to form a

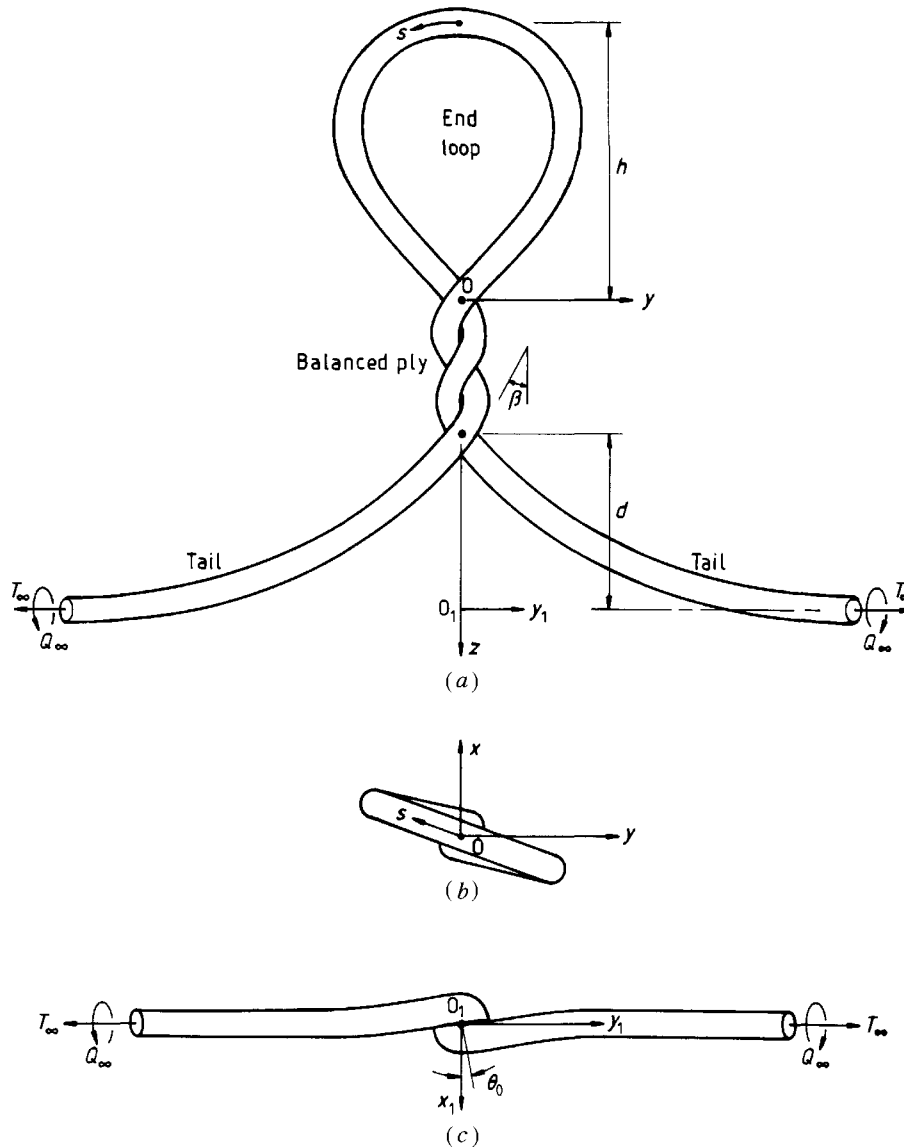


Figure 1. General view of the writhed rod: (a) side elevation; (b) plan view from above the end loop with the tails omitted; (c) plan view from beneath the tails with the end loop omitted.

small loop. Further inward displacements of the remote ends produce the writhed structure shown in figure 1 (see also figure 6 of Thompson & Champneys 1996), which consists of three parts:

- (1) the *balanced-ply* region where the strands are in contact and exert forces on each other;
- (2) the *end loop* region which is attached to the two strands of the balanced ply and is free from any lateral forces or moments; and
- (3) the *tails* which are attached to the bottom of the balanced ply and extend to the remote region of constant applied T_∞ and Q_∞ .

The objective of this paper is to use the large deflection theory of elastic rods of circular cross-section to find the shape, forces and moments in the three parts of the writhed rod. The range of application of the final solution is extensive since writhing occurs in a large number of applications, from undersea cables (Coyne 1990) to the interwound and toroidal supercoiling of DNA (Calladine & Drew 1992; Bauer *et al.* 1980).

The study is organized as follows. In §2, the mathematical formulation for the shape of the rod is presented along with other model assumptions. In §3 the solution for the balanced-ply region is discussed. Sections 4 and 5 develop the equations and jump conditions for the end loop and tails, respectively. Section 6 details the numerical solution for the end loop, while results of the calculations for the tails and end loop are presented in §7. In §8 these results are applied to the long writhed rod in figure 1 and to the writhing of a closed loop. This section also contains a more detailed discussion of the important topological constraint that influences writhing and compares the model predictions with results on DNA supercoiling and some simple experiments with ropes. Some final remarks are included in §9.

The paper is written in distinct sections so that readers who are less interested in the mathematical details of the solution can proceed directly to §§7 and 8 which present the results of the calculations and the applications. The remainder of the introduction is devoted to a discussion of some background literature in mechanics and DNA. This study is quite lengthy and complete discussions on all of the relevant work (particularly on DNA supercoils) are not appropriate in this paper. Rather, the intent is to place this work within the larger context of literature and research on the subject.

(a) The mechanics background

The theory of bent and twisted rods of arbitrary cross-section has a long history and is discussed in ch. 18 of the treatise by Love (1927) where a theory for linear elastic rods that neglects cross-sectional warping is developed. Antman (1995) has summarized many aspects of the general theory in his recent treatise, with particular emphasis on nonlinear constitutive laws and more advanced models such as Cosserat theory.

Thompson & Champneys (1996), Champneys & Thompson (1996) and Champneys *et al.* (1997) have studied the buckling and post-buckling of straight elastic rods subject to equal and opposite torque and tension end loads but with no lateral forces. They have primarily investigated the chaotic solutions which develop for non-circular cross-sections and for nonlinear materials. While they have obtained experimental pictures of writhed rods in lathe fixtures, they have not actually obtained a mathematical description of the shape. It is their experimental results which have partially motivated this study.

A number of other investigators (Coleman & Dill, 1992; Coleman *et al.* 1993; Dichmann & Maddocks 1994) have studied the mathematical structure of the dynamical equations of elastic rods free of lateral forces and moments. These results contain a rigorous theory formulated in terms of a set of principal cross-sectional inertia axes, which is applicable to rods of arbitrary cross-sectional shape. Since this study considers only circular cross-sections, a simpler theory based upon the Frenet basis vectors is sufficient for the mathematical description of the rod.

The analysis of this paper is based upon the work of Fraser & Stump (1998a–c) and Stump & Fraser (1998), who have applied the theory of bent and twisted rods to the static and dynamic analysis of textile yarn-plying processes in which straight yarn segments are plied into a helical structure. At the convergence point where the straight strands come together with the helical portions, the introduction of concentrated forces and moments between the strands is necessary in order to maintain overall structural equilibrium and continuity. This formulation is applied at the two convergence points in the writhed elastic rod where the strands enter and exit the balanced-ply region and is essential to the development of a solution for the writhed shape.

(b) *The DNA background*

The writhing of DNA strands into larger coiled structures is a process known as *supercoiling* and has attracted intense interest due to the importance of supercoils during the transcription and replication processes. Bauer *et al.* (1980), Calladine & Drew (1992) and Wang (1982) have presented non-specialist discussions of the process. Supercoils are formed when DNA loops of the order of μm in size are operated on by a variety of enzymes (e.g. gyrase and topoisomerases) which remove or insert turns of twist relative to the relaxed double-strand structure of approximately 10.2–10.4 base pairs (BP hereafter) per helical turn of the phosphate backbones. The removal or insertion of twist strains the strand, which responds by writhing into a structure that is described approximately by a balanced ply and two end loops (see figure 7). One of the objectives of this paper is to develop a simple analytic formula (without the need for electron micrographs) for predicting the gross features of the shape of the writhed molecule given the degree of under- or over-twisting of the DNA loop.

The methods by which supercoiling catalyses interactions with various enzymes are beyond the scope of this study. The articles by Wang (1982, 1995) and Wang & Liu (1990) describe the role of supercoiling in detail and present various mechanistic models. It is hoped the results of this study will provide further illumination to the interaction of supercoils and topoisomerases.

The mathematical study of DNA supercoiling has primarily used a topological approach to categorize the various supercoiled shapes that preserve the total link inserted into a looped strand of the molecule. The work of White (1969), Fuller (1971, 1978) and Crick (1976) proved instrumental to the development of the understanding that link is conserved and divided into writhe and twist during the coiling process. Much of the history of development of the topological understanding of DNA supercoiling is summarized in the review article by Cozzarelli *et al.* (1990). The related subject of knot theory has also contributed to the understanding of splicing reactions and is discussed by Murasugi (1996).

A variety of mechanics studies of supercoiling ranging from molecular dynamics to finite element continuum models have been undertaken. Recent review articles by Schlick (1995) and Olson (1996) summarize many of the investigations. The article by Schlick shows results (figure 3, p. 250) for supercoiled shapes computed by molecular dynamics techniques that are remarkably similar to the continuum model developed in this study. The advantage of the molecular approach is the ability to incorporate many different effects such as electrochemical forces and thermal agitation, which are

absent from the continuum approach. However, this comes at the expense of any simple formula for relating the gross features of the supercoiled shape to the degree of undertwisting and other parameters. Many of these studies are concerned with DNA behaviour on much shorter length scales than is appropriate for the strictly continuum rod model of supercoiling; although Marko (1997*a*) has recently adapted free-energy minimization techniques to consider the plectonemic (interwound) supercoiling of μm size molecules from a thermodynamic standpoint.

The bibliographies of Schlick (1995) and Olson (1996) indicate a paucity of continuum analyses of interwound supercoiling relative to the molecular approaches. Le Bret (1979) conducted a highly simplified analysis to consider the stability of an elastic ring with trapped twist. Calladine (1980, 1992) has considered toroidal supercoiling and the implications of DNA sequence on the elastic behaviour from a heuristic standpoint using the principles of solid mechanics. Tobias & Olson (1993) and Manning *et al.* (1996) have considered smaller-scale effects of BP variations on the local intrinsic curvature of a relaxed strand of DNA and the consequences that these variations will have on the distribution of twist and writhe along the strand. These latter effects are on a length scale much smaller than is considered here. This analysis is a continuum model applicable to the supercoiling of a long (i.e. several thousand BP) closed loop of DNA, such as those shown in electron micrographs in ch. 6 of Calladine & Drew (1992) and in Wang (1995).

The finite-element method has also been used to predict DNA supercoiling. Yang *et al.* (1993) have used Kirchhoff beam elements to model the writhing of a loop that has differential twist inserted between the two ends. Their results include a variety of realistic loop shapes, but their analysis provides no way of predicting the gross features of the supercoiled molecule shape (such as the supercoil helix angle or the length of the balanced-ply segments) for specified levels of link. Bauer *et al.* (1993) have also used the finite-element method to study the effects that local regions of initial curvature have on the supercoiling of a circular ring.

Finally, it is important to note that molecular dynamics techniques (see, for example, Marko & Siggia 1994, 1995; Marko 1997*b*) have been used in conjunction with experiments on single strands of DNA (see, for example, Smith *et al.* 1996; Wang *et al.* 1997; Strick *et al.* 1996) to predict and measure the elastic behaviour of DNA molecules. As summarized in Austin *et al.* (1997), the uncoiling of the DNA helical strand structure only becomes significant for forces in excess of 10 pN, which are well above the force levels predicted in this analysis. For the purposes of modelling a large supercoil (i.e. μm in size), the assumption of inextensibility proves quite reasonable (as shown in § 8).

2. The mathematical formulation

(a) The model assumptions

The rod is modelled as a strand of uniform circular cross-section and inextensible centreline. Linear bending moment–curvature and torque–torsion constitutive laws are assumed. Since the cross-section is circular, the problem can be formulated entirely in terms of the Frenet derivatives of the centreline.

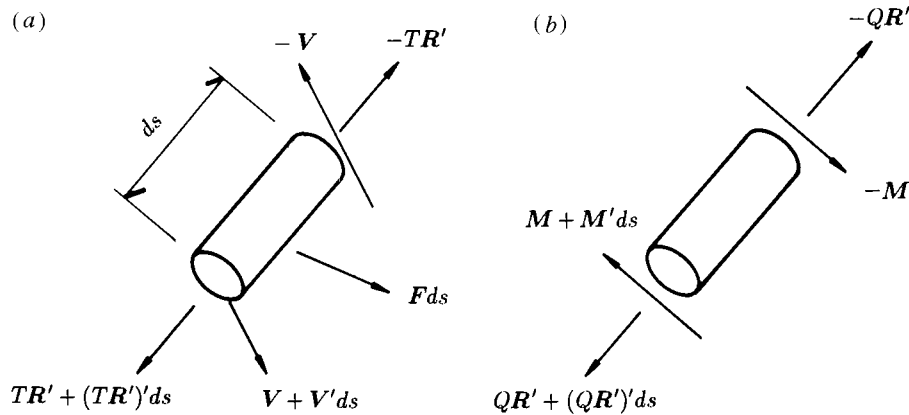


Figure 2. (a) The forces acting on a rod element: the tension T in the tangential direction and a perpendicular shear force V . (b) The moments acting on a rod element: the torque Q in the tangential direction and the bending moment M in the binormal direction \mathbf{b} .

The equations for the bending and torsional stiffnesses, B and K , of a circular shaft of radius a are

$$K = \frac{1}{2}GAa^2, \quad B = \frac{1}{4}EAa^2, \quad (2.1)$$

where E is Young's modulus, G is the shear modulus and $A = \pi a^2$ is the cross-sectional area. If ν is Poisson's ratio, then $G = E/[2(1 + \nu)]$, and

$$\kappa = K/B = 1/(1 + \nu). \quad (2.2)$$

The important point is that the ratio K/B depends only on ν and is $O(1)$.

Let $\mathbf{R}(s)$ be the position vector of a material point of the strand axis with respect to the origin O of the Cartesian coordinate system $Oxyz$ in figure 1. The arc-length coordinate s is measured from the midpoint of the end loop. Since the shape is symmetric about the \mathbf{k} -axis running between the strands, it is only necessary to consider the region $s \geq 0$; the shape for $s \leq 0$ is obtained by a rotation of 180° about the \mathbf{k} -axis.

The centreline of the inextensible rod forms the Frenet basis vector system \mathbf{R}' , $\mathbf{n} = \mathbf{R}''/|\mathbf{R}''|$, and $\mathbf{b} = \mathbf{R}' \wedge \mathbf{n}$ which are, respectively, the tangent, principle normal and binormal of the path, where $(\)' = \partial/\partial s$. The forces and moments acting on an element of the rod are shown in figures 2a, b and consist of: the tension force T and the torque Q in the direction of the tangent \mathbf{R}' ; the bending moment M in the direction of the binormal \mathbf{b} ; and the shear force V lying in the plane formed by the principle normal \mathbf{n} and the binormal \mathbf{b} . \mathbf{F} is the applied force exerted on the element.

Within the balanced-ply region the strands are in contact and exert forces upon each other. The model allows for both frictional and pressure contact forces on the strand surfaces. However, this study makes the simplifying assumption that the centreline of each strand within the balanced ply is described by the shape of a uniform helix of constant winding angle. The translational invariance of the helical shape along the ply axis allows only an effective pressure contact force which is perpendicular to both the ply axis and the strand axes. This is certainly not the only solution for the strand shape within the balanced ply, but the assumption of no friction within

the ply due to the constant helix angle provides the most tractable approach for a first analysis.

(b) *The governing equations*

The formulation of the equations follows that in Fraser & Stump (1998a). In terms of dimensionless quantities defined in equation (2.7), the equations of force and moment equilibrium for the strand $s > 0$ are

$$\left. \begin{aligned} (T\mathbf{R}')' + \mathbf{V}' - p\mathbf{n}[H(s-L) - H(s-l)] + f_h\mathbf{n}\delta(s-L) + f_t\mathbf{n}\delta(s-l) &= \mathbf{0}, \\ (Q\mathbf{R}')' + \mathbf{M}' + \mathbf{R}' \wedge \mathbf{V} + m_h\mathbf{n}\delta(s-L) + m_t\mathbf{n}\delta(s-l) &= \mathbf{0}, \end{aligned} \right\} \quad (2.3)$$

where $H(s)$ is the Heaviside unit step function, $\delta(s)$ is Dirac's delta function, $-p\mathbf{n}$ is the pressure per unit strand length exerted by one strand on the other within the balanced ply, and L and l are, respectively, the locations where the strand enters the balanced ply from the end loop and exits the ply into the tails.

The concentrated forces f_h and f_t , and moments m_h and m_t , point in the principle normal direction \mathbf{n} which lies within the xy -plane of rotational symmetry and represent the resultant forces and moments that the two strands exert on each other at the convergence points at the ends of the balanced ply (shown by the heavy dots in figure 1a). As discussed in Fraser & Stump (1998a), the deformation of the strands at the convergence points is highly three dimensional and therefore only approximately represented by the one-dimensional rod theory. Since the pressure and frictional stresses between the strands vary rapidly in the vicinity of the convergence point over a distance that is less than the strand diameter, only the resultant forces and moments associated with the stress distributions can be taken into account in the context of a one-dimensional rod theory. These are represented as a point force and moment acting in the normal direction between the strands at the convergence point.

The equations of equilibrium are supplemented with the inextensibility constraint and the condition of normality between shear force \mathbf{V} and the axial tension $T\mathbf{R}'$:

$$\mathbf{R}' \cdot \mathbf{R}' = 1, \quad \mathbf{V} \cdot \mathbf{R}' = 0. \quad (2.4)$$

As in Fraser & Stump (1998a, b), N' is the rate of tangential angular rotation of an orthogonal material coordinate system ($\mathbf{e}_1 = \mathbf{R}'$, \mathbf{e}_2 , \mathbf{e}_3) embedded in the cross-section and is obtained from the torsion vector

$$\frac{\partial N}{\partial s} \mathbf{R}' = (\phi' - \mathbf{n} \cdot \mathbf{b}') \mathbf{R}'. \quad (2.5)$$

The torsion can be divided into two components:

- (1) ϕ' , which is the rate of change in angle between the material axes ($\mathbf{e}_1 = \mathbf{R}'$, \mathbf{e}_2 , \mathbf{e}_3) and the Frenet basis vectors (\mathbf{R}' , \mathbf{n} , \mathbf{b}); and
- (2) the tortuosity $-\mathbf{b}' \cdot \mathbf{n}$, which results from the osculation of the plane of curvature.

The linear bending moment–curvature and the torque–torsion constitutive laws are

$$\mathbf{M} = \mathbf{R}' \wedge \mathbf{R}'', \quad Q = \kappa \frac{\partial N}{\partial s}, \quad (2.6)$$

where the ratio $\kappa = K/B$. This completes the set of equations for the static system.

The dimensionless variables used in the equations are related to the physical variables (barred) by the following definitions:

$$\left. \begin{aligned} \mathbf{R} &= \frac{\bar{\mathbf{R}}}{a} = \frac{\bar{x}}{a}\mathbf{i} + \frac{\bar{y}}{a}\mathbf{j} + \frac{\bar{z}}{a}\mathbf{k}, & s &= \frac{\bar{s}}{a}, & p &= \frac{\bar{p}a^3}{B}, \\ T &= \frac{\bar{T}a^2}{B}, & \mathbf{V} &= \frac{\bar{\mathbf{V}}a^2}{B}, & Q &= \frac{\bar{Q}a}{B}, & \mathbf{M} &= \frac{\bar{\mathbf{M}}a}{B}. \end{aligned} \right\} \quad (2.7)$$

(i) *The shear vector*

Formation of the vector product of \mathbf{R}' with $(2.3)_2$ and the use of the triple vector product yields the formula

$$\mathbf{V} = Q(\mathbf{R}' \wedge \mathbf{R}'') + \mathbf{R}' \wedge \mathbf{M}' + m_h \mathbf{b}\delta(s-L) + m_t \mathbf{b}\delta(s-l) \quad (2.8)$$

within all three regions of the writhed rod. Once the rod shape \mathbf{R} is known, \mathbf{M} is computed by $(2.6)_1$, and the additional specification of Q gives the shear \mathbf{V} from (2.8) .

(ii) *Two first integrals*

Formation of the scalar product of \mathbf{R}' with $(2.3)_2$ gives $Q' = 0$ so that Q is a constant throughout the entire rod. In accordance with Mickle & Holmes (1988), the use of (2.8) in $(2.3)_1$ and the formation of the scalar product with \mathbf{R}' , along with the result $\mathbf{V}' \cdot \mathbf{R}' = -\mathbf{V} \cdot \mathbf{R}''$ which follows from $(2.4)_2$, provides

$$T' = -\mathbf{R}'' \cdot \mathbf{R}'''. \quad (2.9)$$

This equation is integrated to obtain

$$T = T_g - \frac{1}{2}|\mathbf{R}''|^2, \quad (2.10)$$

where T_g is a constant that differs in each part of the rod.

(iii) *The elastic strain energy*

The elastic strain energy of the bent and twisted rod is stored in the deformations associated with the torque Q and bending moment \mathbf{M} along the length. The formula for U' , the dimensionless strain energy per unit arc-length, is

$$U' = \frac{Q^2}{2\kappa} + \frac{1}{2}|\mathbf{M}|^2. \quad (2.11)$$

3. The balanced-ply region

The forces and moments within the balanced-ply region have been found as a specialization of a larger study of helically plied yarn structures by Fraser & Stump (1998*a, c*), and aspects of that solution are presented here for completeness. Within the balanced-ply region, the centreline path of strand 1 ($L \leq s \leq l$) is described by the equation of a right-hand helix:

$$\mathbf{R}(s) = \mathbf{i} \cos \theta + \mathbf{j} \sin \theta + \mathbf{k}(s-L) \cos \beta, \quad (3.1)$$

where $\theta = (s - L) \sin \beta$. The equation for strand 2 ($-l \leq s \leq -L$) is obtained by replacing θ with $\theta + \pi$. The Frenet basis vectors of strand 1 are

$$\left. \begin{aligned} \mathbf{R}' &= (-\mathbf{i} \sin \theta + \mathbf{j} \cos \theta) \sin \beta + \mathbf{k} \cos \beta, \\ \mathbf{n} &= -\mathbf{i} \cos \theta - \mathbf{j} \sin \theta, \\ \mathbf{b} &= (\mathbf{i} \sin \theta - \mathbf{j} \cos \theta) \cos \beta + \mathbf{k} \sin \beta. \end{aligned} \right\} \quad (3.2)$$

Substitution of the position vector (3.1) in (2.6)₁, (2.8), and (2.3)₁ determines \mathbf{M} , \mathbf{V} and p in terms of the unknown T and torque Q in each of the helically plied strands:

$$\left. \begin{aligned} \mathbf{M} &= \sin^2 \beta \mathbf{b}, \\ \mathbf{V} &= \{Q \sin^2 \beta - \cos \beta \sin^3 \beta\} \mathbf{b}, \\ p &= T \sin^2 \beta - Q \cos \beta \sin^3 \beta + \sin^4 \beta \cos^2 \beta. \end{aligned} \right\} \quad (3.3)$$

The overall tension T_0 and torque Q_0 acting in the \mathbf{k} -direction through the cross-sectional centre of a helical ply structure are expressed in terms of the two sets of strand variables (denoted by subscript 1 and 2) by

$$\left. \begin{aligned} T_0 \mathbf{k} &= T(\mathbf{R}'_1 + \mathbf{R}'_2) + \mathbf{V}_1 + \mathbf{V}_2 \\ &= \{2T \cos \beta + 2Q \sin^3 \beta - 2 \cos \beta \sin^4 \beta\} \mathbf{k}, \\ Q_0 \mathbf{k} &= \mathbf{M}_1 + \mathbf{M}_2 + Q(\mathbf{R}'_1 + \mathbf{R}'_2) \\ &\quad + T(\mathbf{R}_1 \wedge \mathbf{R}'_1 + \mathbf{R}_2 \wedge \mathbf{R}'_2) + \mathbf{R}_1 \wedge \mathbf{V}_1 + \mathbf{R}_2 \wedge \mathbf{V}_2 \\ &= \{2T \sin \beta + 2Q \cos^3 \beta + 2 \sin^3 \beta (1 + \cos^2 \beta)\} \mathbf{k}. \end{aligned} \right\} \quad (3.4)$$

Since the balanced ply is attached to the end loop which is free from external forces and moments, the overall cross-sectional force and moment $T_0 = Q_0 = 0$. The solution of (3.4) for the unknown strand quantities T and Q and the use of these in (3.3) gives the formulae

$$\left. \begin{aligned} T &= p = \frac{\sin^4 \beta}{\cos 2\beta}, \quad Q = -\frac{2 \cos \beta \sin^3 \beta}{\cos 2\beta}, \\ \mathbf{V} &= -\frac{\cos \beta \sin^3 \beta}{\cos 2\beta} \mathbf{b}, \quad \mathbf{M} = \sin^2 \beta \mathbf{b}, \end{aligned} \right\} \quad (3.5)$$

for the forces and moments in the balanced-ply strands. For later reference, note that the constant elastic energy storage per unit arc-length in each of the balanced-ply strands obtained from (2.11) and (3.5) is

$$U' = \frac{1}{2\kappa} \sin^4 \beta (\tan^2 2\beta + \kappa). \quad (3.6)$$

Two points about the balanced-ply solution deserve mention. First, the solution is completely specified by the helix angle β so that the attached end loop and tails are also expected to be completely described by the angle β . Second, the formulae in (3.5) show that various quantities become unbounded as β approaches 45° . It does not appear possible that β in a balanced ply can be made to approach the critical 'lock-up' value of 57.52° for an incompressible strand material.

4. The end-loop region

In this section the equations for the shape of the end loop are formulated along with a set of jump conditions that must be satisfied between the end loop and ply at the convergence point $s = L$.

(a) The governing equations for end-loaded rods

In the loop and tail regions, the rod is subject only to end loads so that the equilibrium equations (2.3) reduce to

$$\left. \begin{aligned} (TR')' + V' &= \mathbf{0}, \\ (QR')' + M' + R' \wedge V &= \mathbf{0}. \end{aligned} \right\} \quad (4.1)$$

The integral of (4.1)₁ gives

$$TR' + V = C, \quad (4.2)$$

where C is a constant vector which represents the constant total force on any cross-section of the end-loaded rod. This equation is solved for V and inserted into (4.1)₂, which is then integrated to obtain

$$QR' + M = D - R \wedge C, \quad (4.3)$$

where D is a constant moment vector. This equation also has a simple physical meaning since the left side is the total moment on any cross-section of the end-loaded rod.

The differential equation for the end-loaded rod is obtained by replacing M with (2.6)₁, then forming the cross product of R' with (4.3), and finally using the triple vector product identity to derive

$$R'' = R' \wedge (R \wedge C - D). \quad (4.4)$$

This equation must be integrated with a suitable set of boundary conditions for prescribed C and D . Through a linear transformation of R , equation (4.4) can be changed into a coordinate system in which the C and D are parallel and each have only a single component. The integration can then be accomplished in closed form and yields a general solution in terms of elliptic functions, which are transformed back to the original coordinate system. However, since the values of C and D are unknown, the necessary coordinate transformation cannot be specified *a priori*, and it is simpler to integrate numerically the equation system in the original coordinates.

Once R has been found, the forces and moments in the loop are found as follows. The scalar product of R' with (4.2) is formed, and the result is back-substituted in (4.2) to obtain

$$T = C \cdot R', \quad V = C - R'(C \cdot R'). \quad (4.5)$$

Similarly, the scalar product of R' with (4.3) yields

$$Q = R' \cdot (D - R \wedge C), \quad (4.6)$$

which is back-substituted into (4.3) to obtain M . Alternatively, M is available directly from (2.6)₁.

Expression (4.5)₂ for \mathbf{V} is completely consistent with (2.8) as the use of the force and moment expressions for the end-loaded rod in (2.8) produces an identity. In addition, since (2.10) and (4.5)₁ are equivalent, this gives the formula

$$T_g = \mathbf{C} \cdot \mathbf{R}' + \frac{1}{2} |\mathbf{R}''|^2 \quad (4.7)$$

for the constant T_g within the end-loaded segment.

An expression for the elastic energy storage per unit arc-length in the end-loaded rod is found by substitution of (2.6)₁ and (4.7) into (2.11) to obtain

$$U' = \frac{Q^2}{2\kappa} + \frac{1}{2} |\mathbf{R}''|^2 = \frac{Q^2}{2\kappa} + T_g - \mathbf{R}' \cdot \mathbf{C}. \quad (4.8)$$

(b) *The jump conditions*

The Cartesian coordinate system used to describe the shape of the end loop coincides with the convergence point of the balanced ply and end-loop regions (see figure 1). The loop extends for an unknown height h in the $-\mathbf{k}$ -direction, where the origin of the coordinate s is placed, and occupies the domain $-L \leq s \leq L$. Since the end loop is symmetric about the \mathbf{k} -axis, the vectors \mathbf{C} and \mathbf{D} must lie within the xy -plane so that the axial force and moment components C_z and D_z are zero.

The geometric boundary conditions on the loop are given by the continuity of the position and tangent vectors with those of the balanced ply at the two ends. These are obtained from (3.1) and (3.2)₁ as

$$\left. \begin{aligned} \mathbf{R}(-L) &= -\mathbf{i}, & \mathbf{R}'(-L) &= \mathbf{j} \sin \beta - \mathbf{k} \cos \beta, \\ \mathbf{R}(L) &= \mathbf{i}, & \mathbf{R}'(L) &= \mathbf{j} \sin \beta + \mathbf{k} \cos \beta. \end{aligned} \right\} \quad (4.9)$$

The integration of the equilibrium equations (2.3) across the convergence point from L^- to L^+ gives the jump equations

$$[\mathbf{V}] + f_h \mathbf{n} = \mathbf{0}, \quad [\mathbf{M}] + m_h \mathbf{n} = \mathbf{0}, \quad (4.10)$$

where the jump notation $[\mathbf{V}]$ denotes $\mathbf{V}(L^+) - \mathbf{V}(L^-)$ and the continuity of T and Q has been used. The form of the jump equations (4.10) shows that forces and moments at the convergence point are continuous in the tangential and binormal directions and discontinuous in the normal direction where the contact force and moment f_h and m_h act to pry the end loop apart.

Next, the balanced-ply quantities (3.5) and the end loop quantities obtained from (4.2) and (4.3) are substituted into (4.10) to get

$$\left. \begin{aligned} -\frac{\cos \beta \sin^3 \beta}{\cos 2\beta} \mathbf{b} - C_x \mathbf{i} - C_y \mathbf{j} + \frac{\sin^4 \beta}{\cos 2\beta} \mathbf{R}' + f_h \mathbf{n} &= \mathbf{0}, \\ \sin^2 \beta \mathbf{b} - D_x \mathbf{i} - D_y \mathbf{j} + C_y \mathbf{k} - \frac{2 \cos \beta \sin^3 \beta}{\cos 2\beta} \mathbf{R}' + m_h \mathbf{n} &= \mathbf{0}, \end{aligned} \right\} \quad (4.11)$$

where the basis vectors are evaluated at the convergence point $s = L$. Equations (3.1) and (3.2) allow (4.11) to be separated into Cartesian components and yield the four independent jump conditions

$$\left. \begin{aligned} C_x &= -f_h, & C_y &= \frac{\sin^3 \beta}{\cos 2\beta}, \\ D_x &= -m_h, & D_y &= -\frac{\cos \beta \sin^2 \beta}{\cos 2\beta}, \end{aligned} \right\} \quad (4.12)$$

so that only the two constants C_x and D_x (or equivalently the point force f_h and point moment m_h) are unknown. The final problem for the free loop consists of the integration of the vector differential equations (4.4) subject to the boundary conditions (4.9), which is solved with a shooting method to determine C_x , D_x and L for given β . The details of the numerical solution are discussed in § 6.

5. The tail regions

The coordinate system used to describe the tail region is shown in figure 1. The origin O_1 of the axes system $O_1x_1y_1z$ lies a distance d along the \mathbf{k} -axis beneath the convergence point where the tails join the balanced ply. The y_1 -axis of the system is orientated to coincide with the direction of the remote applied tension and torque for the strand with $s > l$. All vector quantities in this section refer to this coordinate system, and the subscript notation is dropped hereafter. In this region the analytic solution first derived by Coyne (1990) can be used as is now shown.

(a) Integration of the governing equations

Equations (4.2) and (4.3) for the end-loaded rods derived in § 4a also apply to the tail regions. However, in the tail region it is possible to determine the constants of integration \mathbf{C} and \mathbf{D} as follows: first note that in the limit $s \rightarrow \infty$, the position, tangent and curvature vectors approach the asymptotes $\mathbf{R} = s\mathbf{j}$, $\mathbf{R}' = \mathbf{j}$ and $\mathbf{R}'' = \mathbf{0}$, respectively, and the forces and moments approach the remote values

$$T = T_\infty, \quad Q = Q_\infty, \quad \mathbf{V} = \mathbf{M} = \mathbf{0}. \quad (5.1)$$

When these results are substituted into equations (4.2) and (4.3) the constants of integration are found to be

$$\mathbf{C} = T_\infty\mathbf{j}, \quad \mathbf{D} = Q_\infty\mathbf{j}, \quad (5.2)$$

so that equation (4.4) becomes

$$\mathbf{R}'' = \mathbf{R}' \wedge (\mathbf{R} \wedge T_\infty\mathbf{j} - Q_\infty\mathbf{j}). \quad (5.3)$$

The integration of this equation is most easily accomplished in terms of the cylindrical-polar coordinates (ρ, α, y) which are related to the $Oxyz$ coordinates shown in figure 1 by the transformation equations

$$x = \rho \sin \alpha, \quad y = y, \quad z = \rho \cos \alpha, \quad (5.4)$$

and

$$\mathbf{R}(s) = \rho(s)\mathbf{e}_\rho[\alpha(s)] + y(s)\mathbf{j}, \quad (5.5)$$

where $(\mathbf{e}_\rho, \mathbf{e}_\alpha, \mathbf{j})$ are the unit basis vectors of the cylindrical-polar coordinate system. The three components of equation (5.3) corresponding to these coordinates are

$$\rho'' - \rho\alpha'^2 = T_\infty\rho y' - Q_\infty\rho\alpha', \quad \rho\alpha'' + 2\rho'\alpha' = Q_\infty\rho', \quad y'' = -T_\infty\rho\rho'. \quad (5.6)$$

Equation (5.6)₂ can be integrated if it is first multiplied by ρ to yield

$$(\rho^2\alpha')' = (\tfrac{1}{2}\rho^2)'Q_\infty. \quad (5.7)$$

This equation is now integrated twice to give

$$\alpha = \tfrac{1}{2}Q_\infty s + \alpha_0, \quad (5.8)$$

where the constant from the first integration is shown to be zero because in the limit $s \rightarrow \infty$, $\rho \rightarrow 0$ and α' must be bounded; α_0 is the second constant of integration.

Equation (5.6)₃ is integrated once to give

$$y' = 1 - \frac{1}{2}T_\infty\rho^2, \quad (5.9)$$

where the constant of integration has been determined from the limit $s \rightarrow \infty$, $y' \rightarrow 1$.

When (5.8) and (5.9) are substituted back into equation (5.6)₁ a second-order differential equation for ρ is obtained:

$$\rho'' - \frac{1}{4}\gamma^2\rho + \frac{1}{2}T_\infty^2\rho^3 = 0, \quad (5.10)$$

where $\gamma^2 = 4T_\infty - Q_\infty^2$ must be non-negative for the validity of the solution derived below. When this equation is multiplied through by ρ' it can be integrated to give

$$\rho'^2 - \frac{1}{4}\gamma^2\rho^2 + \frac{1}{4}T_\infty^2\rho^4 = C, \quad (5.11)$$

where C is a constant of integration, which is seen to be zero when it is noted that in the limit $s \rightarrow \infty$, $\rho \rightarrow 0$ and $\rho' \rightarrow 0$. On rearrangement (5.11) becomes

$$\rho' = -\frac{1}{2}T_\infty\rho\sqrt{(\gamma^2/T_\infty^2) - \rho^2}, \quad (5.12)$$

where the negative sign has been taken for the square root because ρ must be a decreasing function of s in the tail region. Finally this first-order differential equation can be integrated by standard techniques to give the result

$$\rho = \frac{\gamma}{T_\infty} \operatorname{sech}\left[\frac{1}{2}\gamma(s - s_0)\right], \quad (5.13)$$

where s_0 is a constant of integration. This result is now substituted into equation (5.9), which on a further integration yields

$$y = s - \frac{\gamma}{T_\infty} \tanh\left[\frac{1}{2}\gamma(s - s_0)\right] + y_0, \quad (5.14)$$

where y_0 is the final constant of integration.

Solutions (5.8), (5.13) and (5.14) must now be joined smoothly to the balanced-ply region at the convergence point $s = l$ so that the position and tangent vectors \mathbf{R} and \mathbf{R}' are continuous functions of s , and the jump conditions derived below are satisfied.

(b) The jump conditions

Referred to the coordinate system shown in figure 1, the shape of the balanced-ply helix (3.1) becomes

$$\mathbf{R} = \mathbf{i} \cos \theta + \mathbf{j} \sin \theta + \mathbf{k}[(s - l) \cos \beta - d], \quad (5.15)$$

where $\theta = (s - l) \sin \beta + \theta_0$, and θ_0 is an unknown offset angle (see figure 1c). The system of Frenet basis vectors at $s = l$ is

$$\left. \begin{aligned} \mathbf{R}' &= -\mathbf{i} \sin \beta \sin \theta_0 + \mathbf{j} \sin \beta \cos \theta_0 + \mathbf{k} \cos \beta, \\ \mathbf{n} &= -\mathbf{i} \cos \theta_0 - \mathbf{j} \sin \theta_0, \\ \mathbf{b} &= \mathbf{i} \cos \beta \sin \theta_0 - \mathbf{j} \cos \beta \cos \theta_0 + \mathbf{k} \sin \beta. \end{aligned} \right\} \quad (5.16)$$

The position vector of the tails is expressed in the Cartesian coordinate system as

$$\mathbf{R} = \mathbf{i}\rho \sin \alpha + \mathbf{j}y + \mathbf{k}\rho \cos \alpha. \quad (5.17)$$

At the convergence point $s = l$, the continuity of the position and tangent vectors can be rearranged to give the five independent equations (only two components of the tangent are independent due to inextensibility)

$$\left. \begin{aligned} \cos^2 \theta_0 + d^2 &= \rho^2, & \sin \theta_0 &= y, & \tan \alpha &= -\frac{\cos \theta_0}{d}, \\ \sin \beta \cos \theta_0 &= 1 - \frac{1}{2} T_\infty \rho^2, & \sin \beta \sin \theta_0 \cos \theta_0 + d \cos \beta &= -\rho \rho', \end{aligned} \right\} \quad (5.18)$$

where α , ρ and y are given by equations (5.8), (5.13) and (5.14), respectively, evaluated at $s = l$.

The force and moment jump conditions at the convergence point are obtained by integration of equations (2.3) from $s = l^-$ to $s = l^+$, which yields

$$[\mathbf{V}] + f_t \mathbf{n} = \mathbf{0}, \quad [\mathbf{M}] + m_t \mathbf{n} = \mathbf{0}, \quad (5.19)$$

where the jump notation introduced in §4 is used. These equations are analogous to (4.10) and imply the continuity of all forces and moments in the tangential and binormal directions at the convergence point.

The values of the various quantities at $s = l^-$ are given by the balanced-ply solution (3.5) and the basis vectors (5.16). The quantities in the tails at $s = l^+$ are obtained from equations (4.2) and (4.3) with \mathbf{C} and \mathbf{D} given by equations (5.2) and \mathbf{R} given by (5.15). With these substitutions, the jump conditions (5.19) become

$$\left. \begin{aligned} T_\infty \mathbf{j} - \frac{\sin^4 \beta}{\cos 2\beta} \mathbf{R}' + \frac{\cos \beta \sin^3 \beta}{\cos 2\beta} \mathbf{b} + f_t \mathbf{n} &= \mathbf{0}, \\ Q_\infty \mathbf{j} - \mathbf{R} \wedge T_\infty \mathbf{j} + \frac{2 \cos \beta \sin^3 \beta}{\cos 2\beta} \mathbf{R}' - \sin^2 \beta \mathbf{b} + m_t \mathbf{n} &= \mathbf{0}. \end{aligned} \right\} \quad (5.20)$$

The separation of these equations into Cartesian components leads to the four independent conditions

$$\left. \begin{aligned} T_\infty \cos \theta_0 &= \frac{\sin^3 \beta}{\cos 2\beta}, & T_\infty d \sin \theta_0 + Q_\infty \cos \theta_0 &= -\frac{\cos \beta \sin^2 \beta}{\cos 2\beta}, \\ T_\infty \sin \theta_0 &= f_t, & Q_\infty \sin \theta_0 - T_\infty d \cos \theta_0 &= m_t. \end{aligned} \right\} \quad (5.21)$$

The continuity and jump equations (5.18) and (5.21) comprise an overdetermined set of nine algebraic equations in eight unknowns ($\alpha_0, y_0, l - s_0, \theta_0, T_\infty, d, f_t, m_t$). However, it is straightforward to reduce the system to a single transcendental equation. First, note that $(5.21)_1$, $(5.21)_2$ and $Q_\infty = Q$, where Q is given by (3.5)₂, are combined to eliminate T_∞ and yield

$$d = \cot \beta \cot \theta_0 (2 \sin \beta \cos \theta_0 - 1). \quad (5.22)$$

Next, $(5.18)_1$ and $(5.21)_1$ are substituted into $(5.18)_4$ to obtain

$$\sin \beta \cos \theta_0 = 1 - \frac{\sin^3 \beta}{2 \cos \theta_0 \cos 2\beta} [d^2 + \cos^2 \theta_0]. \quad (5.23)$$

Equation (5.22) is used to eliminate d from (5.23), which provides a single transcendental equation for θ_0 in terms of β . The solution is found with Newton's method, and the other quantities are obtained by back-substitution into the various expressions in (5.18), (5.21) and (5.22).

6. Numerical solution for the end loop

The numerical solution of the end-loop equations is discussed in this section. In order to simplify the numerical solution and the asymptotic analysis of Appendix A, the various quantities in the problem are rescaled against the dimensionless end-loop half-length L as the characteristic length scale, which makes all the quantities $O(1)$ in the rescaled system. The rescaled coordinates, forces and moments are

$$\tilde{s} = \frac{s}{L}, \quad \tilde{\mathbf{R}} = \frac{\mathbf{R}}{L}, \quad \tilde{\mathbf{Q}} = L\mathbf{Q}, \quad \tilde{\mathbf{D}} = L\mathbf{D}, \quad \tilde{\mathbf{C}} = L^2\mathbf{C}. \quad (6.1)$$

The rescaled differential equation (4.4) has the form

$$\tilde{\mathbf{R}}'' = \tilde{\mathbf{R}}' \wedge (\tilde{\mathbf{R}} \wedge \tilde{\mathbf{C}} - \tilde{\mathbf{D}}), \quad (6.2)$$

where the rescaled constant vectors of §4*a* are

$$\tilde{\mathbf{C}} = i\tilde{C}_x + j\frac{L^2 \sin^3 \beta}{\cos 2\beta}, \quad \tilde{\mathbf{D}} = i\tilde{D}_x - j\frac{L \cos \beta \sin^2 \beta}{\cos 2\beta}. \quad (6.3)$$

The rescaled torque constraint is obtained from (4.6) and (3.5)₂:

$$-\frac{2L \cos \beta \sin^3 \beta}{\cos 2\beta} = \tilde{\mathbf{R}}' \cdot (\tilde{\mathbf{D}} - \tilde{\mathbf{R}} \wedge \tilde{\mathbf{C}}), \quad (6.4)$$

which must be enforced at a single location along the end loop. The transformed boundary conditions (4.9) are

$$\left. \begin{aligned} \tilde{\mathbf{R}}(-1) &= -i/L, & \tilde{\mathbf{R}}'(-1) &= j \sin \beta - k \cos \beta, \\ \tilde{\mathbf{R}}(1) &= i/L, & \tilde{\mathbf{R}}'(1) &= j \sin \beta + k \cos \beta. \end{aligned} \right\} \quad (6.5)$$

For a given β , the system of equations (6.2) and boundary conditions (6.4) and (6.5) comprise a two-point boundary-value problem involving the iterates L , \tilde{C}_x , and \tilde{D}_x . The system is integrated with a fourth-order Runge–Kutta scheme using (6.5)₁ as initial conditions, and with (6.4) and (6.5)₂ serving as constraint equations in a shooting method for the determination of L , \tilde{C}_x and \tilde{D}_x . A high degree of accuracy is required in the integration of (6.2) in order for the Newton–Raphson iteration to converge.

7. Results for the end loop and tails

The results for the calculations of the end loop and tail regions are presented in this section.

(a) The end loop

The end-loop arc-length L is plotted in figure 3 as a function of balanced-ply helix angle β . There are two families of solutions: the upper branch, which consists of *large* loops that lie primarily in the yz -plane (see insert); and the lower branch, which is comprised of *small* loops that lie primarily in the xz -plane (see insert). (Details of these different types of solutions are discussed below.) The curve is a solid line where the contact pressure force at the convergence point is positive and dashed where it is negative. Along the upper branch of figure 3, L is very sensitive to β , while on

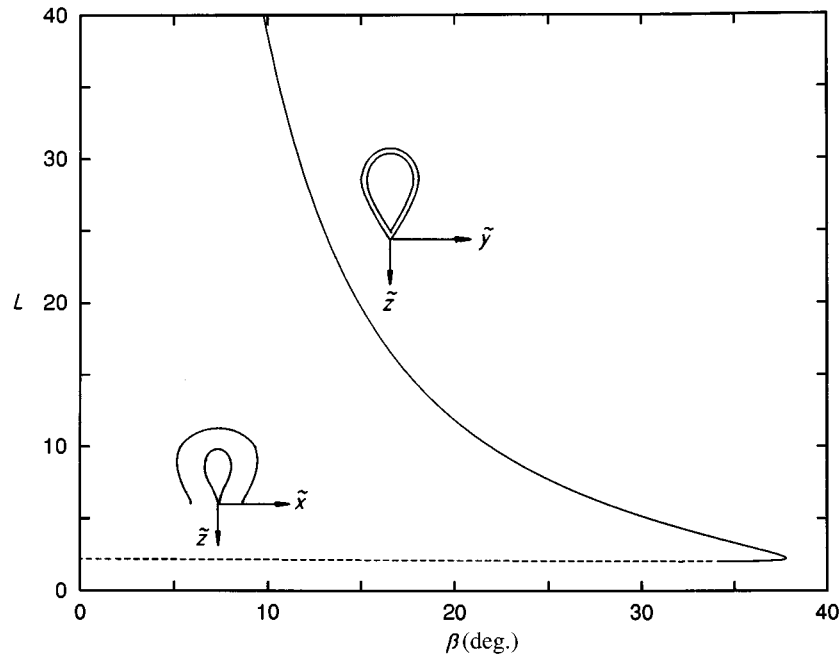


Figure 3. A plot of dimensionless end-loop half-length L versus the helix angle β of the balanced ply.

the lower branch L is almost a constant value independent of β . Interestingly, the diagram shows a turning point at the value $\beta = 37.792^\circ$ beyond which no solution is possible. In the region $34.1^\circ \leq \beta \leq 37.792^\circ$, there are two solutions consistent with positive contact pressure.

(i) *Large loops*

The upper branch of figure 3 is associated with loops that become unbounded in size as $\beta \rightarrow 0$. The asymptotic analysis in Appendix A shows that on the upper branch $L \sim 3.14/\beta^{3/2}$ (β in radians) as $\beta \rightarrow 0$, while the loop shape normalized by L remains well behaved and lies primarily in the yz -plane. Figure 4a shows the $\tilde{y}\tilde{z}$ -plane projection of large loops corresponding to the values $\beta = 0^\circ, 10^\circ, 20^\circ$ and 30° . The asymptotic shape for $\beta \rightarrow 0$ is expressed in terms of elliptic functions in Appendix A.

Since large loops are associated exclusively with the physically realistic case of positive contact pressure where the ends of the loop act to pry each other apart, these are the shapes that would normally be observed in experimental models. The strong sensitivity of L to β is noteworthy since this implies that considerable care will need to be taken in the experimental verification of this curve.

(ii) *Small loops*

The lower branch of figure 3 is associated with the domain $2.04 \leq L \leq 2.24$ and has a finite limit as $\beta \rightarrow 0$. Most of the lower branch of figure 3 is shown as a dashed line representing a contact tension, which is physically unrealistic since it implies

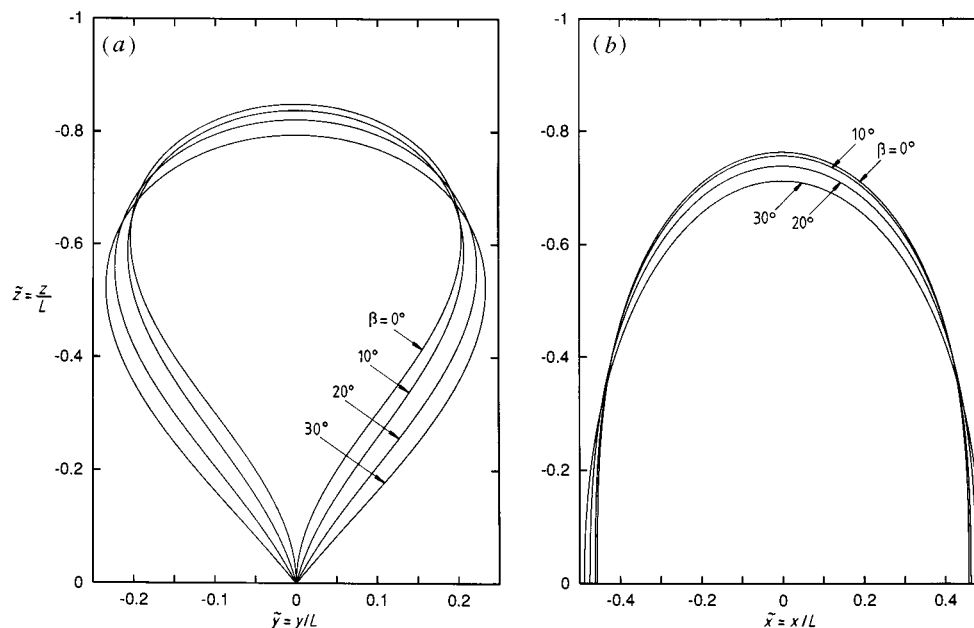


Figure 4. (a) The yz -plane projection of large loops rescaled by the loop length L for various values of β . (b) The xz -plane projection of small loops rescaled by the loop length L for various values of β .

that the ends of the loop are pulling each other together. Figure 4b shows the $\tilde{x}\tilde{z}$ -plane projection of the centreline for the small loops associated with $\beta = 0^\circ, 10^\circ, 20^\circ$ and 30° . The shape for $\beta = 0^\circ$ is also expressed in terms of elliptic functions in Appendix A. It should be noted that the small size of these loops means that most of the space inside the curves of figure 4b is occupied by the rod itself.

(iii) The dimensions

The introduction of the rescaled quantities in § 6 has the effect of making all dimensions $O(1)$ in the $\tilde{\mathbf{R}}$ coordinates so that the essential physical size-scaling behaviour in β is contained in figure 3. However, the relative height and width of the loops are also of interest. (Throughout the remaining plots in this section, solid lines and dashed lines are used to indicate positive and negative contact pressures, respectively.) The loop height $\tilde{h} = h/L = -z(0)/L$ is plotted as a function of β in figure 5a. The height as a proportion of the length L varies between 0.70 and 0.85 for both large and small loops. The asymptotic limit for the large loops is $\tilde{h} = 0.8486$, while the limit for small loops is $\tilde{h} = 0.7628$. The value $\tilde{h} \sim 0.83$ for large loops. It is somewhat surprising that \tilde{h} is relatively insensitive to β .

The maximum projected widths $\tilde{w}_x = w_x/L$ and $\tilde{w}_y = w_y/L$ in the x and y directions are shown as functions of β in figure 5b. Since the loop shape changes from lying primarily in the yz -plane on the upper branch of figure 3 to lying mainly in the xz -plane on the lower branch of figure 3, the widths \tilde{w}_x and \tilde{w}_y approach zero for large and small loops, respectively. The non-zero asymptotes are given by $\tilde{w}_x \sim 0.9139$ and $\tilde{w}_y \sim 0.4084$, which are found from the two asymptotic shapes

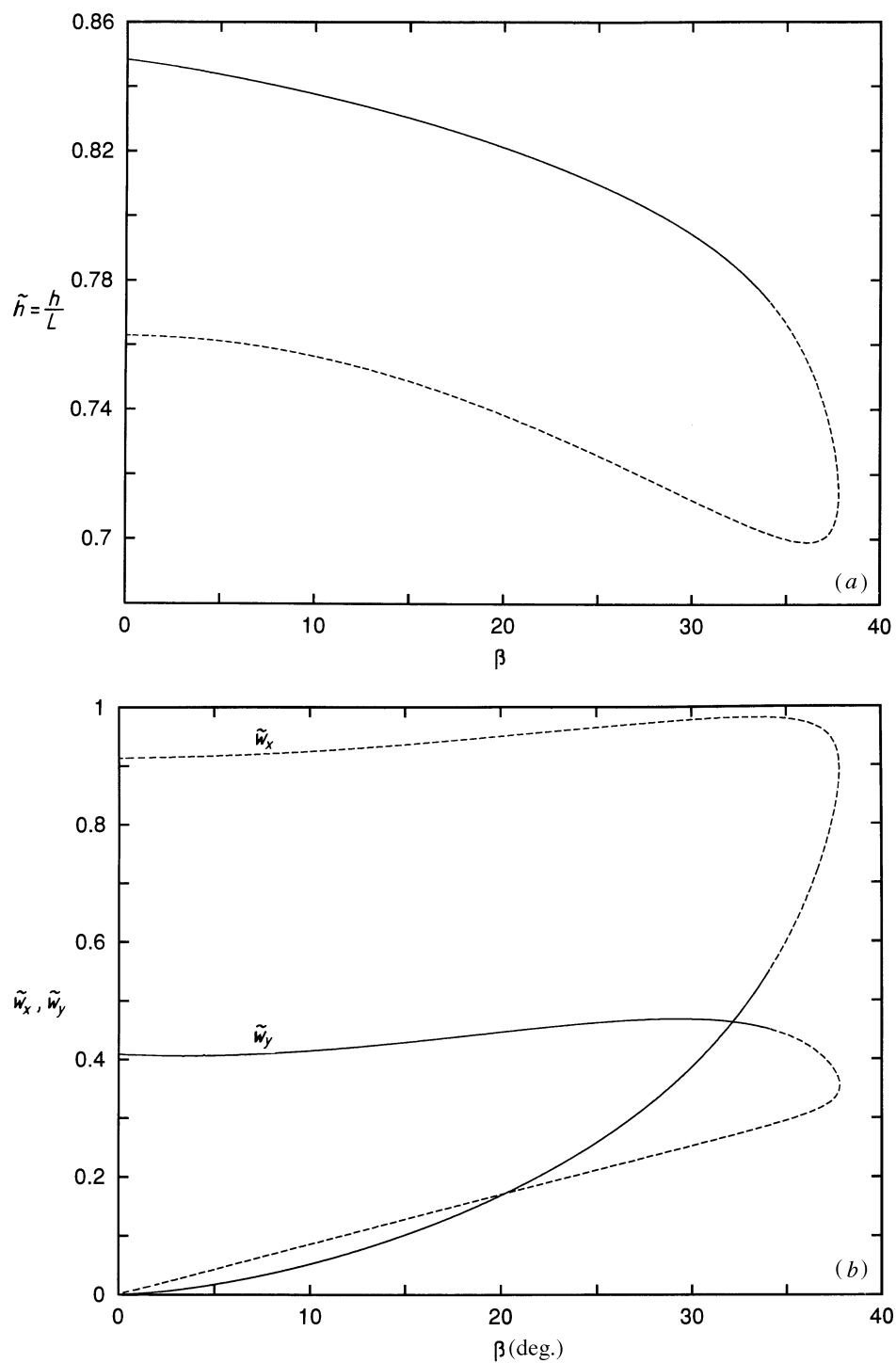


Figure 5. (a) The rescaled loop height \tilde{h} versus β . (b) The rescaled maximum x - and y -direction widths \tilde{w}_x and \tilde{w}_y versus β .

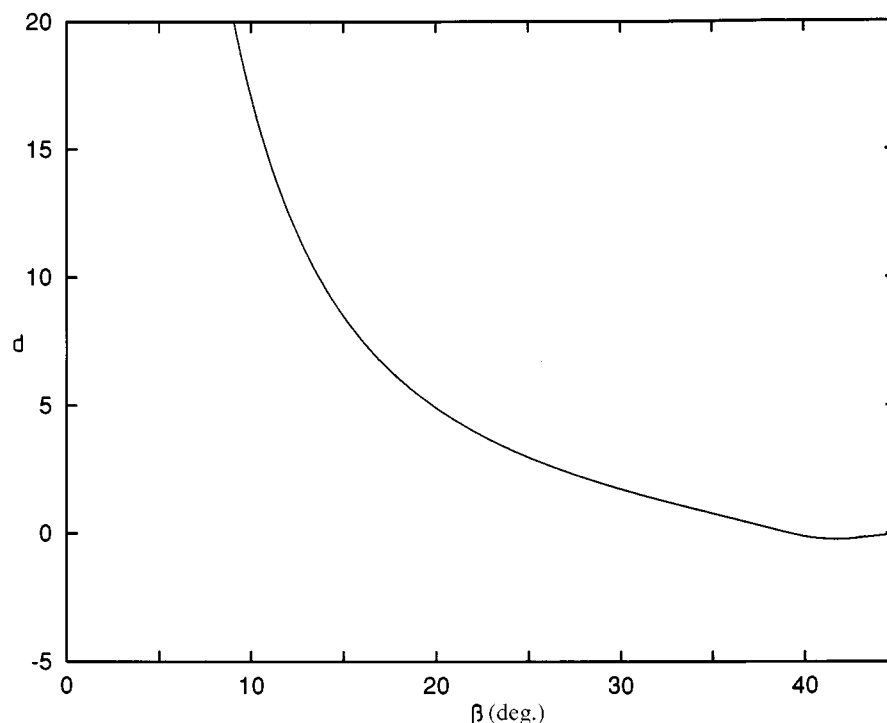


Figure 6. A plot of d , the height of the convergence point above the tails, versus β .

shown in figure 4. The values of \tilde{w}_x and \tilde{w}_y are remarkably constant over the lower and upper branch, respectively, of figure 3. This behaviour in combination with the height behaviour of figure 5a indicates that the loop shape does not vary much along the two branches of figure 3, even though the arc length L of large loops is very sensitive to β .

(b) The tail regions

The solution for the rod shape in the tail regions developed in § 5 is closed form and is joined to the balanced-ply solution by a set of continuity and jump conditions. The three quantities of physical interest from the solution are the remote tension T_∞ , the torque $Q_\infty = Q$ and the height d of the convergence point above the line of action of the remote tension and torque (see figure 1). These are given respectively by (5.21)₁, (3.5)₂ and (5.22).

The height of the tails is shown in figure 6 where d has been plotted against β . As $\beta \rightarrow 0$, the height d diverges while both T_∞ and Q approach zero. The value of d drops to only a few rod radii for helix angles of $20^\circ \leq \beta \leq 35^\circ$, and even becomes slightly negative in the region $42^\circ \leq \beta \leq 45^\circ$ before approaching zero as $\beta \rightarrow 45^\circ$.

8. Application of the results

The results of the elastic rod model are applied to the writhing of closed loops and long elastic rods.

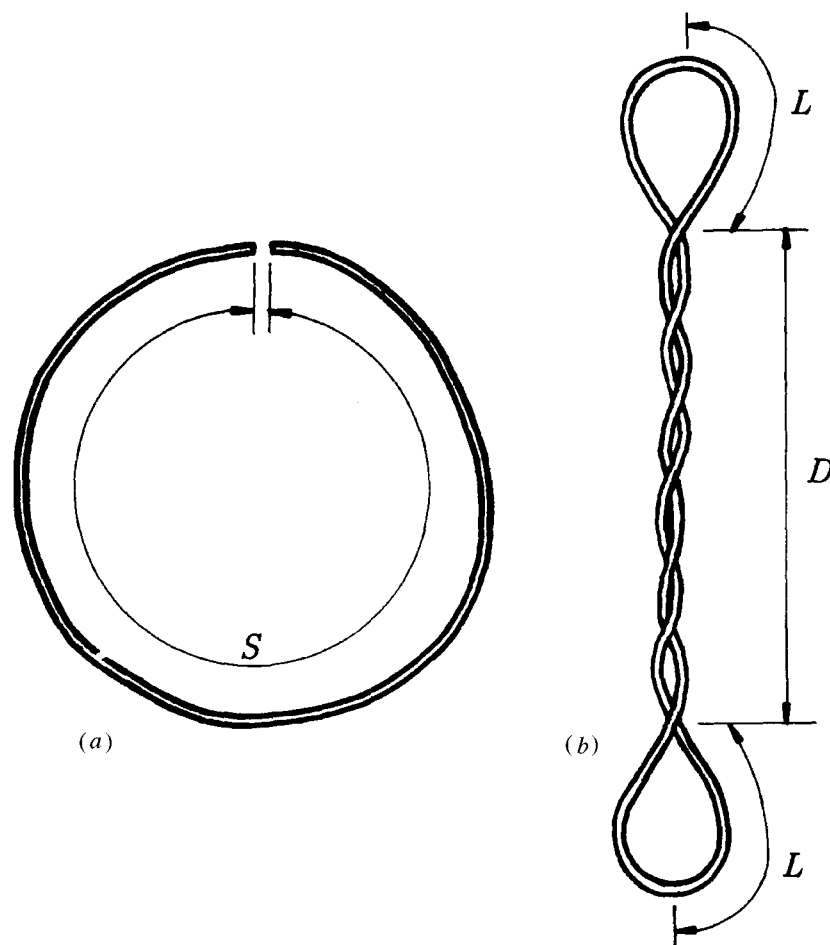


Figure 7. (a) The circular loop of DNA with n turns of twist inserted between the end. (b) The same strand in a writhed configuration with ply length D and end-loop half-length L .

(a) *The closed loop*

Consider the planar closed rod shown in figure 7a. Start with the rod in a straight unstressed reference configuration and draw a straight black line along one side of the cylinder. Next, bend the rod into a circle and twist the two ends relative to one another. After $-n$ integral turns (left-hand rotation is negative in the coordinate system used here), connect the two ends so that the black line forms a continuous curve on the surface of a torus.

When a sufficient number of turns are inserted into the planar loop, it becomes unstable and must be restrained on the table by applied forces. Once these forces are removed, the loop writhes into a shape which consists (at least approximately) of a series of balanced plies and end loops. Figure 7b shows the case of a single balanced ply connected to two end loops and is used as a basis for calculations throughout this section unless stated otherwise.

A model consisting of balanced-ply and end-loop segments developed in the preceding sections is applied to predict the writhed shape of figure 7b for a given number

of inserted turns n and specified arc length S . This is an important problem in the study of DNA supercoiling, and the restriction that arises from the trapping of the inserted turns is discussed first.

(i) *Link, twist and writhe*

The writhing of closed loops of underwound DNA due to the trapped turns has been considered by a number of investigators (White 1969; Fuller 1971; Crick 1976; Bauer *et al.* 1980; Pohl 1980). An important conservation equation which applies to the closed loop of figure 7*b* is reviewed here. More complete discussions and derivations can be found in the references.

The *link* Lk is the number of differential turns inserted between the two loop ends prior to their closure. For figure 7*b*, $Lk = -n$. The link is invariant throughout the writhing process. The formal proof of this assertion (see, for example, Fuller 1971) is based upon topological properties of the centreline and the reference line drawn on the surface of the rod.

The *topological twist* Tw is related to the rotation of the surface reference line about the centreline of the strand and can be obtained from the integration of the rotation rate N' between the two joined ends of the closed loop. For a writhed state with a constant Q along the strand, which includes writhed loops constructed from the balanced-ply and end-loop segments developed here, the integration of (2.6)₂ gives the formula

$$Tw = \frac{N(S) - N(0)}{2\pi} = \frac{QS}{2\pi\kappa}. \quad (8.1)$$

The topological twist Tw is not constant as the closed loop writhes. This can be verified by a simple experiment with a piece of string held between the fingers under fixed end rotation. As the fingers are displaced towards one another and the string writhes into a shape similar to figure 1, the torque, hence Tw , decreases noticeably. In the examples discussed here, the link is given an integral value. However, the topological twist Tw as computed from (8.1) need not have an integral value in a writhed state even though the ends of the reference line remain joined together. Finally, it should be noted that the terminology *topological twist* Tw is different from the textile twist $\phi'/2\pi$ which has been discussed in Fraser & Stump (1998*a-c*) and Stump & Fraser (1998).

The *writhe* Wr is defined to be the difference between Lk and Tw :

$$Wr = Lk - Tw, \quad (8.2)$$

and, as explained by Fuller (1971), it is a property of just the strand centreline. The writhe Wr is a measure of the overall 'curviness' of the path when viewed from the embedding space. Pohl (1980) defines the writhe number Wr of any closed curve by the formula

$$Wr = \frac{1}{4\pi} \oint_{s_1} \oint_{s_2} \mathbf{R}'(s_1) \wedge \mathbf{R}'(s_2) \cdot \frac{\mathbf{R}(s_1) - \mathbf{R}(s_2)}{|\mathbf{R}(s_1) - \mathbf{R}(s_2)|^3} ds_2 ds_1, \quad (8.3)$$

which involves a double integral over the path of the centreline.

Fuller (1978) has given an interpretation of this formula for 'simple' closed paths (i.e. non-knotted) by translating the instantaneous tangent vector to the centre of a unit sphere and then calculating the spherical surface area within the image curve

traced by the tangent as the closed loop is traversed. The formula obtained from applying Fuller's approach to this particular problem is

$$Wr + 1 = \frac{A}{2\pi}, \quad (8.4)$$

where A is the total spherical surface area (which may be positive or negative) enclosed within the image. (It is straightforward to extend this formula to other paths, see Fuller (1978).) This formula is used in Appendix B to determine the writhe of figure 7b.

(ii) *The constraint equations*

The two fundamental restrictions relating the circular and writhed states of figure 7 are the constancy of arc length and the constancy of link. The requirement of fixed arc length is given by the equation

$$\frac{2D}{\cos \beta} + 4L = S, \quad (8.5)$$

where D is the axial length of the balanced-ply segment and L is the half arc-length of each end loop. L depends only on β and can be predicted with good accuracy by using the asymptotic series developed in Appendix A in combination with a numerical scheme to fit the upper branch of figure 3 with a polynomial in powers of $\beta^{k/2}$ where $k = (-3, -2, -1, \dots)$. The four-term series (β in radians)

$$L = \frac{3.1489}{\beta^{3/2}} - \frac{0.1365}{\beta} - \frac{1.041}{\beta^{1/2}} - 1.375 \quad (8.6)$$

is quite accurate for $\beta \leq 0.55$ (31.5°). (It should be remembered that all lengths are dimensionless with respect to the rod radius in accordance with the formulae of (2.7).)

The second fundamental equation is obtained from (8.2) by setting $Lk = -n$. For writhed loops constructed from the balanced-ply and end-loop solutions developed in the previous sections, the value of Q is given by $(3.5)_2$ so that the twist formula (8.1) becomes

$$Tw = -\frac{S \cos \beta \sin^3 \beta}{\pi \kappa \cos 2\beta}. \quad (8.7)$$

This is a new expression because it contains information from the continuum mechanics analysis of the writhed shape, which has not been considered in previous studies. In Appendix B, (8.4) is used as a basis for calculating the writhe expression

$$Wr = -\frac{D}{\pi} \sin \beta + F_{\text{loop}} - 1. \quad (8.8)$$

The factor $F_{\text{loop}} = A_{\text{loop}}/2\pi$, where A_{loop} is the surface area on the unit sphere swept out by the tangent during the traversal of the two end loop segments, is plotted as a function of β in figure 8. The solid line shows the writhe associated with large loops on the upper branch of figure 3, and using the asymptotic analysis of Appendix A it is well approximated by the five-term series (β in radians and $\beta \leq 0.55$)

$$F_{\text{loop}} = -0.4355\beta^{1/2} - 10.87\beta^{3/2} + 56.11\beta^2 - 89.27\beta^{5/2} + 49.22\beta^3. \quad (8.9)$$

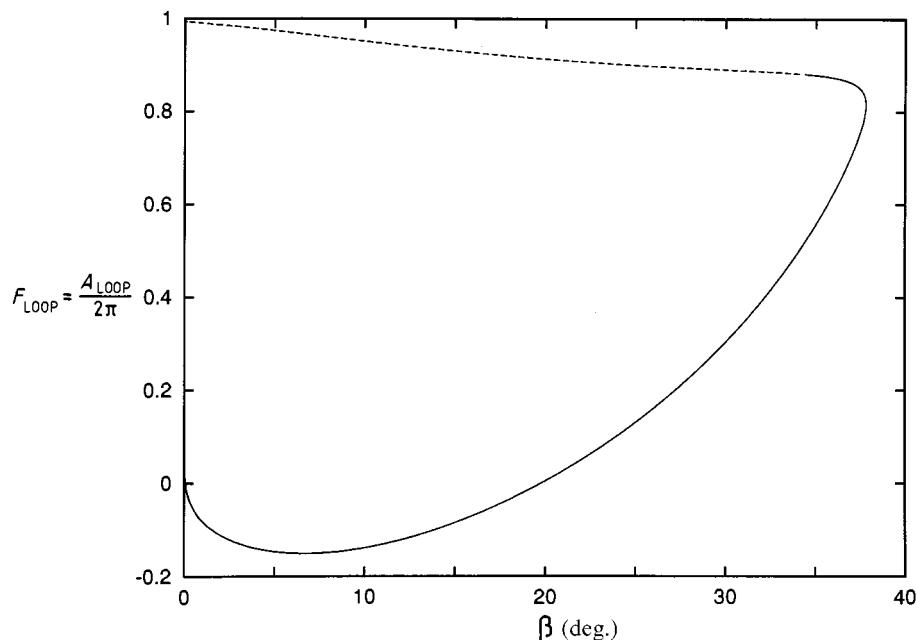


Figure 8. A plot of the spherical area factor $F_{\text{loop}} = A_{\text{loop}}/2\pi$ for a set of end loops versus β .

With these expressions for twist and writhe, the equation for constancy of link is

$$-n = -\frac{S \cos \beta \sin^3 \beta}{\pi \kappa \cos 2\beta} - \frac{D}{\pi} \sin \beta + F_{\text{loop}} - 1. \quad (8.10)$$

The use of (8.5) to eliminate D provides the single transcendental equation for the conservation of link in terms of β :

$$n = \frac{S \cos \beta \sin^3 \beta}{\pi \kappa \cos 2\beta} + \frac{(S - 4L)}{2\pi} \cos \beta \sin \beta - F_{\text{loop}} + 1. \quad (8.11)$$

Once β is determined, the length of the balanced ply, the twist and the writhe are computed from (8.5), (8.7) and (8.8). The formula (8.11) is now applied to several examples.

(iii) Applications of the formula

A 110 cm length of braided 5 mm radius rope was given 25 turns of left-hand twist and then closed. When the external forces were released, the rope writhed into a shape similar to figure 7*b* with 12 crossovers in the balanced-ply segment, a helix angle of approximately 25° and end-loop half-lengths of 4.5 cm. The formula (8.11) is used to predict β using $n = 25$, $S = 110/0.5 = 220$, $\kappa = \frac{2}{3}$ and gives $\beta = 26^\circ$. Back-substitution yields $Tw = -12.3$, $Wr = -12.7$, $D = 86$ and $L = 7.3$. (The dimensional values of the two lengths are $\bar{D} = 43$ cm and $\bar{L} = 3.7$ cm.) The ratio of the balanced-ply axis length to the overall loop length is $D/S = 0.39$, and the number of strand crossovers in the ply is given by $2D/\lambda = D \sin \beta/\pi = 12$, which agree well with the rope data. The model predictions are in quite reasonable agreement with simple experiments considering the high helix angle and the assumption of linear

constitutive laws. The difficulty in defining where the end loop begins and ends makes a direct comparison with the calculations uncertain. More rigorous experiments using Nitinal shape memory alloy are planned.

As a second example, the DNA loop on p. 126 of Calladine & Drew (1992) is analysed. They quote a strand length of 7000 BP and approximately 40 turns of underwinding. The circular loop contains about 660 turns so that the removal of 40 turns represents an underwinding of 6%. The assumptions of a strand radius $a = 10 \text{ \AA}$ and the axial separation distance 3.2 \AA/BP gives a dimensionless strand length $S = 2240$. The formula (8.11) is adjusted to account for the micrograph shape which shows four end loops rather than the two assumed in the derivation and yields $\beta \sim 7.5^\circ$ for the value $\kappa = \frac{2}{3}$. Back-substitution gives $Tw = -2.5$, $Wr = -37.5$, $D = 869$ and $L = 61$. The lengths correspond to the physical dimensions $\bar{D} = 8690 \text{ \AA}$ and $\bar{L} = 610 \text{ \AA}$. In terms of BPs, the axial length of the balanced ply is 2700 BP and the *total* length of each end loop is 380 BP. The ratio of the balanced-ply axis length to the overall loop length is $D/S = 0.39$, which is the same as for the simple experiment with the twisted rope. Finally, the number of strand crossovers in the balanced ply is given by $2D/\lambda = D \sin \beta/\pi = 36$, which corresponds to approximately 150 BP for each wavelength of the balanced-ply helix.

These results are comparable with those of Calladine & Drew (1992) who estimate $Wr = -36$ by counting the number crossovers and infer $Tw = -4$ from the constancy of link. Given that the actual link of the strand is unknown and the relatively low forces and moments from (3.5) opposing the electrostatic repulsion of the phosphate backbones along the strand, the model results are in reasonable agreement with the experimental inferences.

Cozzarelli *et al.* (1990) have presented a model of supercoiling based upon experimental measurements. They assert that the ratio of $D/S = 0.41$ (their l/L) remains unchanged over a wide range of relative undertwisting (2–12%). This certainly agrees with the two examples. However, their model is more complicated since it accounts also for the electrostatic repulsion of the strands, and they present evidence (figure 16, p. 171) that the strands in the balanced ply do not actually touch but are separated from each other by a distance that depends upon the degree of specific linking difference (i.e. percentage underwinding). They also assert that the pitch of the superhelix (their γ which is the complement of β) is constant at $\gamma = 54^\circ$ over the same range of undertwisting. This angle corresponds to a $\beta = 36^\circ$ in our system, which is significantly greater than our prediction based upon contacting strands. However, these results can be understood with this simpler model as follows.

First, the model developed here is the simplest approach and does not include any electrostatic repulsion due to the phosphate groups along the backbone so that the strands within the ply are in direct physical contact. The pressure p between the strands is given in terms of β by (3.5)₁, and results from direct contact. This model can be extended to include a pressure term due to electrostatic repulsion, which would predict a stable structure with a stand-off distance related to the helix angle β .

Second, Cozzarelli *et al.* (1990) report that the stand-off distance is the only variable that changes significantly with increased underwinding; the angle γ and the superhelix wavelength λ remain essentially constant (see their figure 15, p. 169 for a sketch of several shapes.) If these experimental facts are accepted then the model developed here can be adapted to describe the stand-off effect by drawing two right triangles with λ as the hypotenuse. One triangle relates the model parameters λ ,

β , and $2\pi a$ for strands in contact, while the other relates λ , γ , and $2\pi r$, for the non-contact model. The constancy of λ between the two models means that

$$\frac{2\pi a}{\sin \beta} = \frac{2\pi r}{\cos \gamma}.$$

This expression along with figure 16 of Cozzarelli *et al.* (1990) allows for conversion between models by pulling the strands apart and changing the apparent helix angle while keeping the other features of the model the same. Consider the value of $\gamma = 54^\circ$ for the example of 6% underwinding described above, for which Cozzarelli *et al.* (1990) predict a stand-off distance of $r = 50 \text{ \AA}$. For the value $a = 10 \text{ \AA}$, the conversion formula predicts $\beta = 6.7^\circ$, which is consistent with the contact model value of $\beta = 7.5^\circ$. Essentially, the electrical repulsion pushes the strands apart and increases the pitch to compensate without altering the other features of the model. (The end-loop length will also change, but this is a much smaller adjustment.)

Several points deserve further mention. First, with the energy density expressions U' developed for the end loop and balanced ply, it is straightforward to show that the energy stored in the writhed shape is lower than the circular configuration. Second, the issue of whether a particular loop writhes into a single balanced ply connected to two end loops or into a more complicated arrangement with a larger number of end loops and balanced plies could be answered in part by comparing the overall elastic energy contained in the various possible writhed shapes constructed from this model. However, this would only yield an approximate qualitative picture due to the limitations of the uniform elastic rod model of DNA. It is highly likely that any regions of local weakness in the strand (such as ATAT rich segments) also contribute to nucleating end loops. Third, the strand tension \bar{T} computed for the DNA example above can be calculated from (2.7), the value $E \sim O(10^8) \text{ N m}^{-2}$ (Austin *et al.* 1997), $\beta = 7.5^\circ$, and $a = 10^{-9} \text{ m}$ and is predicted to be $\bar{T} \sim 0.03 \text{ pN}$, which is well below the 10 pN level needed to extend the BP separation distance within the double-stranded helical structure. This verifies the assumption of inextensibility.

(b) The long elastic rod

The results are now applied to describe the long straight rod loaded by remote tension and torque. Since the tail solution depends upon $s \rightarrow \infty$, examine an infinitely long straight rod subjected to a fixed remote applied torque Q_∞ and to an adjustable remote tension T_∞ , as is shown figure 9a. Consider how this structure develops into the writhed rod, and note that there are an infinite number of turns in the rod.

When the tension T_∞ is reduced to $\frac{1}{4}Q_\infty^2$ the rod buckles, and under increasing T_∞ the Coyne (1990) solution develops, which is given here by (5.8), (5.13) and (5.14) with the constants of integration all set equal to zero. An interesting aspect of the Coyne solution is that the inward displacement of each point at infinity,

$$\Delta_T = \lim_{s \rightarrow \infty} \frac{1}{2}[y(s) - y(-s)] = -\frac{2}{T_\infty} \sqrt{4T_\infty - Q_\infty^2}, \quad (8.12)$$

increases in opposition to the increasing tension in the range $\frac{1}{4}Q_\infty^2 \leq T_\infty \leq \frac{1}{2}Q_\infty^2$ so that the rod does work against the applied tension load (figure 9b). At $T_\infty = \frac{1}{2}Q_\infty^2$, the inward displacement of the Coyne solution reaches its maximum value (figure 9c). Further inward movement of the remote points causes the end loop to flip around dynamically and to contact itself. The precise details of this shape have not been

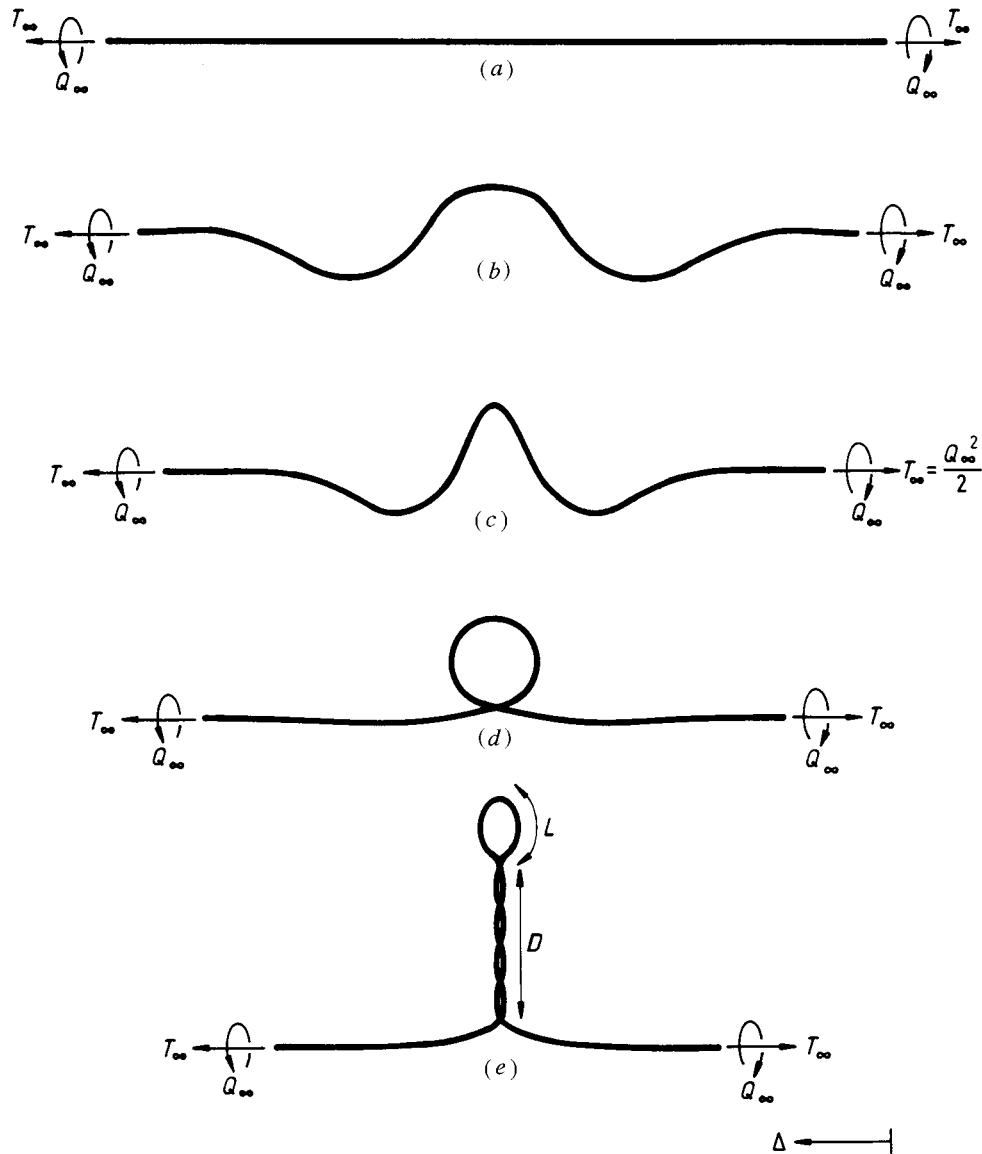


Figure 9. (a) The straight rod under remote tension T_∞ and torque Q_∞ . (b) The rod after buckling and while the Coyne solution applies. (c) The maximum inward displacement of the Coyne solution. (d) The rod just after the contacting loop has formed. (e) The writhed shape that develops under significant inward displacement of the remote ends.

calculated but this can be done in principle by combining the equations of § 4 *a* with the tail analysis of § 5 *a* and then formulating an appropriate set of continuity and jump conditions. The shape of the end loop at first contact is not the same as the end loop attached to the balanced-ply helix so that as the remote points are displaced further inward, there appears to be some sliding of the two strands against each other during the winding up of the helix region. This is a complicated transient process which we have not attempted to model (see figure 9*d*).

After a sufficient amount of remote displacement, the writhed structure shown in figure 9e, and more closely in figure 1, is obtained. The end loop and tails have reached the proper shape and the balanced-ply region has developed. The inward displacement of each remote loading point Δ is absorbed completely by the arc length of the end loop and the balanced ply, which gives the formula

$$\Delta = L + \frac{D}{\cos \beta} \quad (8.13)$$

for D the balanced-ply length. The formulation of the problem has been based on a set of simple experiments with flexible ropes and only limited instrumentation. Verification of the writhing process requires a much more carefully conducted experiment where the remote displacement, rotation, tension and torque can be controlled and measured.

The long-rod analysis has so far considered the case when Q_∞ is held constant throughout the writhing process, which requires the rotation of the remote ends to input extra energy due to the bending of the rod in the writhed state. It is also possible to allow a finite-length rod to writhe after a fixed number of rotations have been inserted between the ends of the straight rod (for example, by locking the rod into a lathe fixture with fixed rotation at the ends). In this case, a form of the link restriction (8.2) applies during the course of writhing. A simple experiment with a piece of rope, say 2 m long, which is made to writhe under fixed end rotations shows that the helix angle of the balanced ply changes noticeably during the fixed-link writhing process (see also figure 6 of Thompson & Champneys (1996)). This requires a more complicated analysis of the balanced-ply region and will be considered in subsequent work.

9. Concluding remarks

The large deflection theory of elastic rods has been used to study two problems of interest: the writhing of closed loops, and the writhing of long elastic rods. The prescription of a balanced-ply region that is a uniform helix means that the shapes of both structures are completely parametrized by the helix angle β .

The model predictions for the writhed shape of closed loops are in approximate quantitative agreement with data obtained from electron microscopy of DNA and simple experiments with ropes. The writhing of the long elastic rod has not been compared with experimental data, but the analysis appears to predict the important features of the final rod shape. Experimental confirmation of both applications remains a priority.

In applying this model to the description of interwound DNA supercoiling, it should be kept in mind that the purpose of (8.11) is to provide a simple predictive tool that captures the gross features of the supercoiled shape rather than to predict the precise strand shape in all circumstances and on all length scales. The model developed here constitutes a theoretical advance since it brings together the continuum mechanics and topological approaches to provide a better understanding of the interaction of the two effects and provides a means for making *quantitative* estimates of supercoil shape.

This work has been supported by an Australian Research Council Large Grant to D.M.S. and W.B.F., and by a grant to W.B.F. from the US National Textile Centre at Clemson University,

South Carolina. Discussions with Charlie Macaskill, Colin Please, Tony Watts, Larry Forbes, John Maddocks, Gert van der Heijden, Mike Thompson, Alan Champneys and Louis Kauffman have been most helpful and appreciated. Mr Stuart Lee assisted with some of the calculations and in the preparation of various figures.

Appendix A. Asymptotic end-loop analysis

The two families of loops associated with $\beta \rightarrow 0$ are considered with perturbation series, but first the complete Cartesian components of the differential equation (6.2) and the torque constraint (6.4) are presented.

The Cartesian components of (6.2) are

$$\left. \begin{aligned} \tilde{x}'' &= \tilde{y}'(\tilde{x}\tilde{C}_y - \tilde{y}\tilde{C}_x) - \tilde{z}'(\tilde{z}\tilde{C}_x - \tilde{D}_y), \\ \tilde{y}'' &= -\tilde{z}'(\tilde{z}\tilde{C}_y + \tilde{D}_x) - \tilde{x}'(\tilde{x}\tilde{C}_y - \tilde{y}\tilde{C}_x), \\ \tilde{z}'' &= \tilde{x}'(\tilde{z}\tilde{C}_x - \tilde{D}_y) + \tilde{y}'(\tilde{z}\tilde{C}_y + \tilde{D}_x), \end{aligned} \right\} \quad (\text{A } 1)$$

where \tilde{C}_y and \tilde{D}_y are given by (6.3). The torque equation (6.4) is

$$-\frac{2L \cos \beta \sin^3 \beta}{\cos 2\beta} = \tilde{x}'(\tilde{D}_x + \tilde{z}\tilde{C}_y) + \tilde{y}'(\tilde{D}_y - \tilde{z}\tilde{C}_x) + \tilde{z}'(\tilde{y}\tilde{C}_x - \tilde{x}\tilde{C}_y). \quad (\text{A } 2)$$

(a) The large loop

The loop shape, forces and moments associated with the upper branch of the L versus β curve shown in figure 3 are obtained by introducing the following perturbation expansions in powers of $\beta^{1/2}$:

$$\left. \begin{aligned} L &= L_{-3/2}\beta^{-3/2} + L_{-1}\beta^{-1} + \dots, \\ \tilde{C}_x &= \tilde{C}_{1/2}\beta^{1/2} + \tilde{C}_1\beta + \dots, \\ \tilde{D}_x &= \tilde{D}_0 + \tilde{D}_{1/2}\beta^{1/2} + \dots, \\ \tilde{x}(\tilde{s}) &= \tilde{x}_{3/2}(\tilde{s})\beta^{3/2} + \tilde{x}_2(\tilde{s})\beta^2 + \dots, \\ \tilde{y}(\tilde{s}) &= \tilde{y}_0(\tilde{s}) + \tilde{y}_{1/2}(\tilde{s})\beta^{1/2} + \dots, \\ \tilde{z}(\tilde{s}) &= \tilde{z}_0(\tilde{s}) + \tilde{z}_{1/2}(\tilde{s})\beta^{1/2} + \dots \end{aligned} \right\} \quad (\text{A } 3)$$

These expansions are substituted into the rescaled equations for the end loop (A 1), the torque equation (A 2), the inextensibility equation (2.4)₁ and the boundary conditions (6.5). The resulting system of equations is then separated into a series of boundary-value problems for different $O(\beta^{n/2})$ with $n = (0, 1, 2, \dots)$. The leading $O(1)$ system of equations is

$$\tilde{y}_0'' = -L_{-3/2}^2 \tilde{z}_0 \tilde{z}_0' - \tilde{D}_0 \tilde{z}_0', \quad \tilde{z}_0'' = \tilde{y}_0' \tilde{z}_0 L_{-3/2}^2 + \tilde{D}_0 \tilde{y}_0', \quad (\tilde{y}_0')^2 + (\tilde{z}_0')^2 = 1. \quad (\text{A } 4)$$

The associated $O(1)$ boundary conditions are

$$\left. \begin{aligned} \tilde{y}_0(-1) &= \tilde{z}_0(-1) = \tilde{y}_0'(-1) = 0, & \tilde{z}_0'(-1) &= -1, \\ \tilde{y}_0(1) &= \tilde{z}_0(1) = \tilde{y}_0'(1) = 0, & \tilde{z}_0'(1) &= 1. \end{aligned} \right\} \quad (\text{A } 5)$$

This system can be integrated in closed form as follows. The integral of (A 4)₁ in combination with the boundary conditions (A 5) gives

$$\tilde{y}'_0 = -\frac{1}{2}L_{-3/2}^2\tilde{z}_0^2 - \tilde{D}_0\tilde{z}_0. \quad (\text{A } 6)$$

The insertion of (A 6) into (A 4)₃ directly or in combination with the integration of (A 4)₂ gives the equation

$$\tilde{z}'_0 = \sqrt{1 - \tilde{z}_0^2[\frac{1}{2}L_{-3/2}^2\tilde{z}_0 + \tilde{D}_0]^2}, \quad (\text{A } 7)$$

which is valid in the region $0 \leq \tilde{s} \leq 1$ since \tilde{z}_0 is an even function of \tilde{s} . With the variable change $\tilde{z}_0 = -u - \tilde{D}_0/L_{-3/2}^2$ the integral of this equation can be put in the form

$$\int_u^b \frac{du}{\sqrt{(c^2 + u^2)(b^2 - u^2)}} = \frac{1}{2}\tilde{s}L_{-3/2}^2, \quad (\text{A } 8)$$

where

$$b^2 = \frac{2}{L_{-3/2}^2} + \frac{\tilde{D}_0^2}{L_{-3/2}^4}, \quad c^2 = \frac{2}{L_{-3/2}^2} - \frac{\tilde{D}_0^2}{L_{-3/2}^4}. \quad (\text{A } 9)$$

This integral has a closed-form representation in terms of Jacobi elliptic functions (equation 17.4.49 of Abramowitz & Stegun (1965)), and the coordinate \tilde{z}_0 is given by

$$\tilde{z}_0 = -b \operatorname{cn}[\tilde{s}L_{-3/2}; m] - \frac{\tilde{D}_0}{L_{-3/2}^2}, \quad (\text{A } 10)$$

where the index $m = b^2/(b^2 + c^2)$. This expression is used in (A 6) which is then integrated (equation 16.26.2 of Abramowitz & Stegun (1965)) to obtain

$$\tilde{y}_0 = \frac{\tilde{s}\tilde{D}_0^2}{2L_{-3/2}^2} - \frac{b^2L_{-3/2}}{2m} \{E[\tilde{s}L_{-3/2}; m] - m_1\tilde{s}L_{-3/2}\}, \quad (\text{A } 11)$$

where $m_1 = 1 - m$ and E is the incomplete elliptic integral of the second kind.

The assertion of the boundary conditions $\tilde{z}_0(1) = 1$ and $\tilde{y}_0(1) = 0$ gives a set of transcendental equations for $L_{-3/2}$ and \tilde{D}_0 which are solved by a Newton–Raphson procedure to obtain $L_{-3/2} = 3.1484$ and $\tilde{D}_0 = 3.0276$.

(b) The small loop

The lower branch of the L versus β plot in figure 3 is associated with a family of end-loop shapes that remain bounded in size as $\beta \rightarrow 0$. This family of solutions is described by introducing the perturbation series expansions in powers of β :

$$\left. \begin{aligned} L &= L_0 + L_1\beta + \dots, \\ \tilde{C}_x &= \tilde{C}_0 + \tilde{C}_1\beta + \dots, \\ \tilde{D}_x &= \tilde{D}_1\beta + \tilde{D}_2\beta^2 + \dots, \\ \tilde{x}(\tilde{s}) &= \tilde{x}_0(\tilde{s}) + \tilde{x}_1(\tilde{s})\beta + \dots, \\ \tilde{y}(\tilde{s}) &= \tilde{y}_1(\tilde{s})\beta + \dots, \\ \tilde{z}(\tilde{s}) &= \tilde{z}_0(\tilde{s}) + \tilde{z}_1(\tilde{s})\beta + \dots \end{aligned} \right\} \quad (\text{A } 12)$$

These expansions are substituted into the rescaled equations for the end loop (A 1), the torque equation (A 2), the inextensibility condition (2.4)₁ and the boundary conditions (6.5) to obtain the leading $O(1)$ system of equations

$$\tilde{x}_0'' = -\tilde{z}_0\tilde{z}_0'\tilde{C}_0, \quad \tilde{z}_0'' = \tilde{z}_0\tilde{x}_0'\tilde{C}_0, \quad (\tilde{x}_0')^2 + (\tilde{z}_0')^2 = 1 \quad (\text{A } 13)$$

and boundary conditions

$$\left. \begin{aligned} \tilde{z}_0(-1) = \tilde{x}_0'(-1) = 0, & \quad \tilde{z}_0'(-1) = -1, & \quad \tilde{x}_0(-1) = -1/L_0, \\ \tilde{z}_0(1) = \tilde{x}_0'(1) = 0, & \quad \tilde{z}_0'(1) = 1, & \quad \tilde{x}_0(1) = 1/L_0. \end{aligned} \right\} \quad (\text{A } 14)$$

The equations (A 13) are integrated as follows. The integral of (A 13)₁ and the boundary conditions (A 14) provide

$$\tilde{x}_0' = -\frac{1}{2}\tilde{C}_0\tilde{z}_0^2, \quad (\text{A } 15)$$

which is then used in (A 13)₃ to obtain

$$\tilde{z}_0' = \sqrt{1 - \frac{1}{4}\tilde{C}_0^2\tilde{z}_0^4} \quad (\text{A } 16)$$

for the region $0 \leq \tilde{s} \leq 1$. With the variable change

$$u = -\tilde{z}_0\sqrt{\frac{1}{2}|\tilde{C}_0|},$$

the integral of this equation is rewritten

$$\int_u^1 \frac{dt}{\sqrt{1-t^4}} = \tilde{s}\sqrt{\frac{1}{2}|\tilde{C}_0|}, \quad (\text{A } 17)$$

and is expressible in terms of elliptic functions (see equation 17.4.52 of Abramowitz & Stegun (1965)) as

$$\tilde{z}_0 = -\sqrt{\frac{2}{|\tilde{C}_0|}} \operatorname{cn}[\tilde{s}\sqrt{|\tilde{C}_0|}; \tfrac{1}{2}]. \quad (\text{A } 18)$$

This expression is inserted into (A 15), which is then integrated to yield

$$\tilde{x}_0 = \frac{2}{\sqrt{|\tilde{C}_0|}} \operatorname{E}[\tilde{s}\sqrt{|\tilde{C}_0|}; \tfrac{1}{2}] - \tilde{s}. \quad (\text{A } 19)$$

The assertion of the boundary condition $\tilde{z}_0(1) = 0$ gives $\tilde{C}_0 = -3.4375$, and the boundary condition $\tilde{x}_0(1) = 1/L_0$ yields $L_0 = 2.1884$.

Appendix B. The writhe of the closed loop

In this appendix the method of Fuller (1978), given by (8.4), is used to calculate the writhe number of a closed curve based upon the spherical surface area traced out by the spherical image (Struik 1961) of the tangent vector. Let the tangent vector $\mathbf{t} = \mathbf{R}'$ have the Cartesian components (t_1, t_2, t_3) and let (r, ω, η) be a coincident spherical coordinate system where ω is the circumferential angle measured from the x -axis and η is the polar angle measured from the z -axis. The spherical basis vectors are

$$\left. \begin{aligned} \mathbf{e}_r &= \mathbf{i} \cos \omega \sin \eta + \mathbf{j} \sin \omega \sin \eta + \mathbf{k} \cos \eta, \\ \mathbf{e}_\omega &= -\mathbf{i} \sin \omega + \mathbf{j} \cos \omega, \\ \mathbf{e}_\eta &= \mathbf{i} \cos \omega \cos \eta + \mathbf{j} \sin \omega \cos \eta - \mathbf{k} \sin \eta. \end{aligned} \right\} \quad (\text{B } 1)$$

Let $\mathbf{t} = \mathbf{e}_r$ so that the angles (ω, η) can be treated as functions of s as the close curve is traced out on the surface of the unit sphere. The spherical basis vectors can also be expressed in terms of the components of \mathbf{t} :

$$\left. \begin{aligned} \mathbf{e}_r &= i t_1 + j t_2 + k t_3, \\ \mathbf{e}_\omega &= \frac{-i t_2 + j t_1}{\sqrt{t_1^2 + t_2^2}}, \\ \mathbf{e}_\eta &= \frac{i t_1 t_3 + j t_3 t_2}{\sqrt{t_1^2 + t_2^2}} - k \sqrt{1 - t_3^2}. \end{aligned} \right\} \quad (\text{B } 2)$$

The element of surface area on the unit sphere is $dA = \sin \eta \, d\eta \, d\omega$, and the area A of a closed curve as measured from the polar axis is

$$A = \oint d\omega \int_0^{\eta(\omega)} \sin \eta \, d\eta = \oint [1 - \cos \eta] \, d\omega, \quad (\text{B } 3)$$

where the angle η has been taken as an implicit function of ω . With the parametrization $0 \leq s \leq s_0$ for the closed curve, (B 3) becomes

$$A = \int_0^{s_0} (1 - \cos \eta) \omega' \, ds, \quad (\text{B } 4)$$

which can be expressed in terms of the components (t_1, t_2, t_3) and their derivatives. From $\mathbf{t} = \mathbf{e}_r$ and $\mathbf{t} \cdot \mathbf{t} = 1$, it is straightforward to obtain

$$\mathbf{t}' = \mathbf{e}_\omega \omega' \sin \eta + \mathbf{e}_\eta \eta', \quad (\text{B } 5)$$

so that

$$\cos \eta = \mathbf{t} \cdot \mathbf{k}, \quad \omega' \sin \eta = \mathbf{t}' \cdot \mathbf{e}_\omega. \quad (\text{B } 6)$$

With (B 5) and (B 6), the area integral (B 4) is given in terms of vector quantities by

$$A = \int_0^{s_0} \sqrt{\frac{1 - \mathbf{t} \cdot \mathbf{k}}{1 + \mathbf{t} \cdot \mathbf{k}}} \mathbf{t}' \cdot \mathbf{e}_\omega \, ds. \quad (\text{B } 7)$$

With (B 2), this can be written out in terms of the Cartesian components

$$A = \int_0^{s_0} \frac{t'_2 t_1 - t'_1 t_2}{1 + t_3} \, ds. \quad (\text{B } 8)$$

Alternate formulations using i or j as the polar axis are obtained by cyclicly permuting the indices $(1, 2, 3)$.

(a) The balanced ply

Within each wavelength $\lambda = 2\pi/\tan \beta$ along the axis of the balanced ply, the tangents of the two strands trace out a counter-clockwise circle at the colatitude β from the polar axis \mathbf{k} and a clockwise circle with a colatitude β measured from $-\mathbf{k}$. The arc length of each strand in an axial wavelength is $s_0 = 2\pi/\sin \beta$. From (3.2) and (B 2), the quantities in (B 6) become

$$\mathbf{t} \cdot \mathbf{k} = \cos \beta, \quad \mathbf{t}' \cdot \mathbf{e}_\omega = \sin^2 \beta. \quad (\text{B } 9)$$

A_1 , the spherical surface area associated with strand 1 which traces out the counter-clockwise circle about the \mathbf{k} -axis, is obtained from using (B 9) in (B 8) to provide

$$A_1 = \int_0^{2\pi/\sin\beta} (1 - \cos\beta) \sin\beta \, ds = 2\pi(1 - \cos\beta), \quad (\text{B } 10)$$

which agrees with Fuller (1978). A similar analysis for strand 2 taking account that the circle traces a clockwise circle around the south pole of the sphere gives the formula

$$A_2 = -2\pi(1 + \cos\beta), \quad (\text{B } 11)$$

which is the negative of the supplementary area to (B 10). The *net* spherical surface area A_λ per axial wavelength of balanced ply is

$$A_\lambda = A_1 + A_2 = -4\pi \cos\beta, \quad (\text{B } 12)$$

which agrees with Tanaka & Takahashi (1985). For a ply length D , the number of turns is D/λ so that total spherical surface area is

$$A_{\text{ply}} = -\frac{D4\pi}{\lambda} \cos\beta = -2D \sin\beta. \quad (\text{B } 13)$$

(b) The end loops

The spherical surface area traced out by each set of ends loops (such as those shown in figure 7*b*) can be calculated by joining the two loops together to form a continuous figure. Since the surface area is independent of the physical coordinate system, it is useful to employ the rescaling of § 6 so that $\mathbf{t} = \tilde{\mathbf{R}}'(\tilde{s})$. The coordinates $\tilde{\mathbf{R}}(\tilde{s})$ of the *upper* loop are denoted by a subscript 'u' and parametrized by $-1 \leq \tilde{s} \leq 1$. The coordinates of the *lower* loop (denoted by a subscript 'l') can be parametrized in the same way and are related to the upper loop coordinates by

$$\tilde{x}_l(\tilde{s}) = -\tilde{x}_u(\tilde{s}), \quad \tilde{y}_l(\tilde{s}) = \tilde{y}_u(\tilde{s}), \quad \tilde{z}_l(\tilde{s}) = -\tilde{z}_u(\tilde{s}). \quad (\text{B } 14)$$

With (B 14), the closed-loop integral (B 8) for the spherical area of the loop A_{loop} becomes

$$A_{\text{loop}} = \int_{-1}^1 \frac{t'_2 t_1 - t'_1 t_2}{1 + t_3} + \frac{t'_1 t_2 - t'_2 t_1}{1 - t_3} \, d\tilde{s} = \int_{-1}^1 \frac{2t_3(t'_1 t_2 - t'_2 t_1)}{1 - t_3^2} \, d\tilde{s}. \quad (\text{B } 15)$$

For numerical reasons it is preferable to permute the indices 1 and 3 so that \mathbf{i} is the polar axis. The subsequent use of the notation of § 6 provides the formula

$$A_{\text{loop}} = \int_{-1}^1 \frac{2\tilde{x}'}{1 - (\tilde{x}')^2} \{\tilde{y}''\tilde{z}' - \tilde{z}''\tilde{y}'\} \, d\tilde{s}, \quad (\text{B } 16)$$

and the use of (A 1) and (A 2) reduces this to

$$A_{\text{loop}} = \int_{-1}^1 \frac{2\tilde{x}'}{1 - (\tilde{x}')^2} \{\tilde{x}'\tilde{Q} - (\tilde{z}\tilde{C}_y + \tilde{D}_x)\} \, d\tilde{s}. \quad (\text{B } 17)$$

Similar formulae using the \mathbf{j} - or \mathbf{k} -axes as poles can be developed from (B 15).

The normalized factor $F_{\text{loop}} = A_{\text{loop}}/2\pi$ is plotted in figure 8. In the limit $\beta \rightarrow 0$ for the large-loop solution, the figure lies in the $\tilde{y}\tilde{z}$ -plane with a single crossover so that the loop writhe Wr_{loop} computed from (8.4) becomes $Wr_{\text{loop}} = -1$. In the limit

$\beta \rightarrow 0$ for the small-loop solutions, the figure forms an open loop in the $\tilde{x}\tilde{z}$ -plane so that $Wr_{\text{loop}} = 0$.

The *total* writhe number of the closed loop is calculated by using the total spherical surface area $A = A_{\text{ply}} + A_{\text{loop}}$ in (8.4) to obtain

$$Wr = -\frac{D}{\pi} \sin \beta + F_{\text{loop}} - 1. \quad (\text{B } 18)$$

References

- Abramowitz, M. & Stegun, I. 1965 *Handbook of mathematical functions*. New York: Dover.
- Antman, S. S. 1995 *Nonlinear problems of elasticity*. Berlin: Springer.
- Austin, R. H., Brody, J. P., Cox, E. C., Duke, T. & Volkmuth, W. 1997 Stretch genes. *Phys. Today* **50**, 32–38.
- Bauer, W. R., Crick, F. H. C. & White, J. H. 1980 Supercoiled DNA. *Sci. Am.* **243**, 100–113.
- Bauer, W. R., Lund, R. A. & White, J. H. 1993 Twist and writhe of a DNA loop containing intrinsic bends. *Proc. Natn. Acad. Sci. USA* **90**, 833–837.
- Calladine, C. R. 1980 Toroidal elastic supercoiling of DNA. *Biopolymers* **19**, 1705–1713.
- Calladine, C. R. 1992 Application of structural mechanics to biological systems. *Theoretical and applied mechanics* (ed. S. R. Bodner *et al.*), pp. 205–219. New York: Elsevier.
- Calladine, C. R. & Drew, H. R. 1992 *Understanding DNA, the molecule and how it works*, ch. 6, pp. 114–137. New York: Academic.
- Champneys, A. R. & Thompson, J. M. T. 1996 A multiplicity of localized buckling modes. *Proc. R. Soc. Lond. A* **452**, 2467–2491.
- Champneys, A. R., van der Heijden, G. H. M. & Thompson, J. M. T. 1997 Spatially complex localization after one-twist-per-wave equilibria in twisted circular rods with initial curvature. *Phil. Trans. R. Soc. Lond. A* **355**, 2151–2174.
- Coleman, B. D. & Dill, E. H. 1992 Flexure waves in elastic rods. *J. Acoust. Soc. Am.* **91**, 2663–2673.
- Coleman, B. D., Dill, E. H., Lembo, M., Lu, Z. & Tobias, I. 1993 On the dynamics of rods in the theory of Kirchhoff and Clebsch. *Arch. Ration. Mech. Analysis* **121**, 339–359.
- Coyne, J. 1990 Analysis of the formation and elimination of loops in twisted cable. *IEEE J. Oceanic Engng* **15**, 72–83.
- Cozzarelli, N. R., Boles, T. R. & White, J. H. 1990 Primer on the topology and geometry of DNA supercoiling. *DNA topology and its biological Effects*, pp. 139–184. Cold Spring Harbor Laboratory Press.
- Crick, F. H. C. 1976 Linking numbers and nucleosomes. *Proc. Natn. Acad. Sci. USA* **73**, 2639–2643.
- Dichmann, D. J. & Maddocks, J. H. 1994 Hamiltonian dynamics of an elastica and stability of solitary waves. *J. Elasticity* **34**, 83–96.
- Fraser, W. B. & Stump, D. M. 1998a The equilibrium of the convergence point in two-strand yarn plying. *Int. J. Solids Struct.* **35**, 285–298.
- Fraser, W. B. & Stump, D. M. 1998b Yarn twist in the ring spinning balloon. *Proc. R. Soc. Lond. A* **454**, 707–723.
- Fraser, W. B. & Stump, D. M. 1998c Twist in balanced-ply structures. *J. Text. Inst.* (In the press.)
- Fuller, F. B. 1971 The writhing number of a space curve. *Proc. Natn. Acad. Sci. USA* **68**, 815–819.
- Fuller, F. B. 1978 Decomposition of the linking number of a closed ribbon: a problem from molecular biology. *Proc. Natn. Acad. Sci. USA* **75**, 3557–3561.

- Greenhill, A. G. 1883 On the strength of shafting when exposed both to torsion and end thrust. *Inst. Mech. Eng. Proc.* **1883**, 182–209.
- Le Bret, M. 1979 Catastrophic variation of twist and writhing of circular DNAs with constraint. *Biopolymers* **18**, 1709–1725.
- Love, A. E. H. 1927 *A treatise on the mathematical theory of elasticity*, 4th edn, ch. 18, pp. 381–398. Cambridge University Press.
- Manning, R. S., Maddacks, J. H. & Kahn, J. D. 1996 A continuum model of sequence dependent DNA structure. *J. Chem. Phys.* **105**, 5626–5646.
- Marko, J. F. 1997a Supercoiled and braided DNA under tension. *Phys. Rev. E* **55**, 1758–1772.
- Marko, J. F. 1997b Stretching must twist DNA. *Europhys. Lett.* **38**, 183–188.
- Marko, J. F. & Siggia, E. D. 1994 Bending and twisting elasticity of DNA. *Macromolecules* **27**, 981–988.
- Marko, J. F. & Siggia, E. D. 1995 Stretching DNA. *Macromolecules* **28**, 8759–8770.
- Miekle, A. & Holmes, P. 1988 Spatially complex equilibria of buckled rods. *Arch. Ration. Mech. Analysis* **101**, 319–348.
- Murasugi, K. 1996 *Knot theory and its applications*, ch. 13, pp. 267–283. Boston, MA: Birkhauser.
- Olson, W. K. 1996 Simulating DNA at low resolution. *Curr. Opin. Struct. Biol.* **6**, 242–256.
- Pohl, W. F. 1980 DNA and differential geometry. *Math. Intelligencer* **3**, 20–27.
- Schlick, T. 1995 Modelling superhelical DNA: recent analytical and dynamic approaches. *Curr. Opin. Struct. Biol.* **5**, 245–262.
- Smith, S. B., Cui, Y. & Bustamante, C. 1996 Overstretching B-DNA: the elastic response of individual double-strand and single strand DNA molecules. *Science* **271**, 795–798.
- Strick, T. R., Allemand, J. -F., Bensimon, D., Bensimon, A. & Croquette, V. 1996 The elasticity of a single supercoiled DNA molecule. *Science* **271**, 1835–1837.
- Struik, D. J. 1961 *Lectures on classical differential geometry*, ch. 1, pp. 1–54. London: Addison-Wesley.
- Stump, D. M. & Fraser, W. B. 1998 On the dynamical theory of twist in yarn plying. *Math. Eng. Ind.* (In the press.)
- Tanaka, F. & Takahashi, H. 1985 Elastic theory of supercoiled DNA. *J. Chem. Phys.* **83**, 6017–6026.
- Thompson, J. M. T. & Champneys, A. R. 1996 From helix to localized writhing in the torsional post-buckling of elastic rods. *Proc. R. Soc. Lond. A* **452**, 117–138.
- Tobias, I. & Olson, W. K. 1993 The effect of intrinsic curvature on supercoiling: predictions of elasticity theory. *Biopolymers* **33**, 639–646.
- Wang, J. C. 1982 Topoisomerases. *Sci. Am.* **247**, 94–109.
- Wang, J. C. 1995 Enzymes that supercoil DNA. *DNA-protein structural interactions* (ed. D. Lilly), pp. 76–87. Oxford University Press.
- Wang, J. C. & Liu, L. F. 1990 DNA replication: topological aspects and the role of DNA topoisomerases. *DNA topology and its biological effects*, pp. 321–340. Cold Spring Harbor Laboratory Press.
- Wang, M. D., Yin, H., Landick, R., Gelles, J. & Block, S. M. 1997 Stretching DNA with optical tweezers. *Biophys. J.* **72**, 1335–1346.
- White, J. H. 1969 Self-linking and the Gauss integral in higher dimensions. *Am. J. Math.* **91**, 693–728.
- Yang, Y., Tobias, I. & Olson, W. 1993 Finite element models of DNA supercoiling. *J. Chem. Phys.* **98**, 1673–1686.